

LOW RATES OF Rock organic carbon oxidation and ANTHROPOGENIC CYCLING OF rhenium IN A SLOWLY DENUDING LANDSCAPE

AUTHORS

Mateja Ogrič¹, Mathieu Dellinger^{1,2,3}, Katherine E. Grant¹, Valier Galy⁴, Xin Gu^{5,6,7}, Susan L. Brantley^{5,6} & Robert G. Hilton^{1,8}

AFFILIATIONS

¹*Department of Geography, Durham University, South Road, DH1 3LE Durham, UK.*

²*Department of Earth Sciences, Durham University, South Road, DH1 3LE Durham, UK.*

³*Environnements DYnamiques et Territoires de la Montagne (EDYTEM), CNRS - Université Savoie Mont-Blanc, 73370 Le Bourget-Du-Lac, France*

⁴*Woods Hole Oceanographic Institution, Department of Marine Chemistry and Geochemistry, Woods Hole, MA 02543, USA.*

⁵*Department of Geosciences, Pennsylvania State, University Park, PA 16802, USA.*

⁶*Earth and Environmental Systems Institute, Pennsylvania State University, University Park, PA 16802, USA.*

⁷*Environmental Sciences Division, Oak Ridge National Laboratory, Oak Ridge, TN 37831, USA.*

⁸*Department of Earth Sciences, University of Oxford, South Parks Rd, Oxford, OX1 3AN, UK*

CORRESPONDING AUTHOR

Mateja Ogrič, ogric.mateja@gmail.com

ACKNOWLEDGEMENTS

The research was funded by the European Commission via a European Research Council Starting Grant "ROC-CO₂" (project 678779) to RGH. Work at Shale Hills is facilitated by the Penn State College of Agricultural Sciences and Department of Ecosystem Science and Management as part of Penn State's Stone Valley Forest. The SSH CZO was funded by National Science Foundation Grant no. EAR 13 31726, 13-31726 to SLB. We thank Jordon Hemingway, Jennifer Williams, and Brandon Forsythe for field work assistance and help with archived samples and databases. We also thank

Amanda Hayton, Martin West and Eleanor Ross for assistance with laboratory work at Durham University.

AUTHOR CONTRIBUTIONS

Conceptualization: MO, MD, RGH

Funding Acquisition: RGH, SLB

Methodology: MO, MD, RGH, KEG, VG, XG

Investigation: MO, XG

Resources: SLB, XG

Supervision: RGH, MD, SLB

Writing – initial draft: MO

Writing – reviewing and editing: MO, MD, KEG, VG, XG, SLB, RGH

DATA AVAILABILITY STATEMENT

All data used for the production of this manuscript can be found in Table 1 and Table 2 within the main text.

57 Abstract

58 The oxidation of petrogenic organic carbon (OC_{petro}) is a source of carbon
59 dioxide to the atmosphere over geological timescales. The rates of OC_{petro}
60 oxidation in locations that experience low rates of denudation remain poorly
61 constrained, despite these landscapes dominating Earth's continental
62 surface area. Here, we track OC_{petro} oxidation using radiocarbon and the
63 trace element rhenium (Re) in the deep weathering profiles, soils and
64 stream waters of the Susquehanna Shale Hills Critical Zone Observatory
65 (PA, USA). In a ridge-top borehole, radiocarbon measurements reveal the
66 presence of a broad OC_{petro} weathering front, with a first order assessment
67 of $\sim 40\%$ loss occurring over ~ 6 m. However, the low OC_{petro} concentration
68 (< 0.05 wt.%) and inputs of radiocarbon throughout the deepest parts of
69 the profile complicate the assessment of OC_{petro} loss. The OC_{petro} weathering
70 front coincides with a zone of Re depletion ($\sim 90\%$ loss), and we estimate
71 that $> 80\%$ of Re in the rock is associated with OC_{petro} , based on Re/Na and
72 Re/S ratios. Using estimates of long-term denudation rates, the observed
73 OC_{petro} loss and the Re proxy are equivalent to a low OC_{petro} oxidation yield
74 of $< 1.7 \times 10^{-2} \text{ tC km}^{-2} \text{ yr}^{-1}$. This is consistent with the low OC_{petro}
75 concentrations and low denudation rates at this location. In addition, we
76 find the surface cycle of Re is decoupled from that of deep weathering, with
77 an enrichment of Re in surface soils and elevated Re concentrations in
78 stream water, precipitation, and shallow groundwater. A mass balance
79 model shows that this can be explained by a historical anthropogenic

contribution of Re through atmospheric deposition. We estimate that the topsoil Re pool could take decades to centuries to deplete and call for a renewed focus on anthropogenic perturbation of the surface Re cycle in low denudation rate settings.

Keywords: *chemical weathering, rock organic carbon, oxidation, rhenium, low denudation, anthropogenic impacts.*

Introduction

The transfer of carbon between biogeochemical reservoirs is one of the main drivers of climate change over geological timescales (Berner and Canfield, 1989; Derry and France-Lanord, 1996). Over long time periods, carbon dioxide (CO₂) emissions through volcanism, carbonate weathering by sulfuric acid, and oxidation of rock-derived organic carbon (petrogenic, OC_{petro}) are countered by CO₂ sequestration through silicate weathering, carbonate formation, and burial of biospheric organic carbon (OC_{bio}) (Hilton and West, 2020). The CO₂ emissions from OC_{petro} oxidation (Petsch, 2014; Gu and Brantley, 2022) and carbonate weathering by sulfuric acid (Torres et al., 2017; Burke et al., 2018) may be of similar magnitude to the release of CO₂ from volcanic degassing (79±9 MtC yr⁻¹, Plank and Manning, 2019), yet the global rates of OC_{petro} oxidation remain poorly constrained (Petsch, 2014).

The oxidative weathering of OC_{petro} has been assessed in river catchments using the trace element rhenium (Re) (Dalai et al., 2002; Hilton et al., 2014, 2021; Horan et al., 2017, 2019). Rhenium is enriched in sediments deposited in reducing conditions, and preserved in sedimentary rocks (Morford et al., 2012), especially in organic carbon-rich black shales (Colodner et al., 1993), due to a close association of Re with organic matter in rocks (Selby and Creaser, 2003). Coupled loss of Re and OC_{petro} has been observed during oxidative weathering (Jaffe et al., 2002; Hilton et al., 2014), with the mobilization of Re in the dissolved load over the large pH range (5.5 to 9.5) and in oxygenated waters ($\text{Eh} > 0 \text{ V}$), typical of most river waters (Colodner et al., 1993). As such, dissolved Re flux has been used as a proxy to estimate catchment-wide OC_{petro} oxidation rates in highly erosive catchments of the Himalaya (Dalai et al., 2002), Taiwan (Hilton et al., 2014) and New Zealand (Horan et al., 2017) and in moderate erosive setting of the Mackenzie River basin (Horan et al. 2019), the European Alps (Hilton et al., 2021) and Pacific Northwest of the USA (Ghazi et al., 2022).

Applying the Re proxy to settings with moderate to high erosion rates has been important for establishing the role of OC_{petro} supply in driving weathering fluxes (Hilton et al., 2014; Horan et al., 2017; Ghazi et al., 2022). However, there are reasons why lower erosion rate settings deserve focus. First, low denudation rates ($< 0.5 \text{ mm yr}^{-1}$) are common over the majority of Earth's continents, and these settings contribute to $\sim 60\%$ of global chemical denudation (Larsen et al., 2014). Second, low erosion rates can lead to the development of thick weathering profiles, helping to reveal

reaction fronts of OC_{petro} and sulfide oxidation (Petsch et al., 2000; Wildman, 2004; Brantley et al., 2013a; Gu and Brantley, 2022) and track the mobility of Re during weathering (Jaffe et al., 2002). Finally, settings with lower chemical denudation could be more sensitive to Re inputs from anthropogenic sources (Miller et al., 2011; Rahaman et al., 2012), helping us understand the modern-day perturbation of the Re cycle (Sen and Peucker-Ehrenbrink, 2012). This is because Re is enriched in fossil fuels (Bertine and Goldberg, 1971; Selby et al., 2007), volatile at temperatures >270 °C (Colodner et al., 1995), and can be deposited from ash fallout after coal combustion. Anthropogenic Re inputs have been invoked to explain high dissolved Re concentrations in large European rivers (Danube, Rhine), the Yangtze and the Mississippi rivers (Miller et al., 2011) alongside lake and marine records from North America (Chappaz et al., 2008; Prouty et al., 2014).

In this study we explore OC_{petro} weathering and the trace element Re in deep shale weathering profiles (~30 m) in an OC-poor and low denudation rate setting to provide estimates of long-term OC_{petro} oxidation rates. Having done so, we provide new constraints on anthropogenic Re perturbation in the near surface environment on a catchment scale.

Methodology and methods

The study is set in the Shale Hills catchment of the Susquehanna Shale Hills Critical Zone Observatory (SSH-CZO). There, a low denudation rate results

in deep weathering profiles (Jin et al., 2010; Brantley et al., 2013; Sullivan et al., 2016; Gu et al., 2020a). We quantify OC_{petro} weathering using a combination of new radiocarbon and Re measurements, with previously published S and major element concentration data (Brantley et al., 2013; Sullivan et al., 2016), applied to samples from subsurface boreholes, surface soils, rainwater and stream water.

Study site

Shale Hills is a small (0.08 km²), first order catchment located in the Appalachia of central Pennsylvania (Figure 1a). The catchment is almost exclusively underlain by Rose Hill Formation of Silurian age, with low total organic carbon (TOC) concentrations of <0.05 wt.% (Jin et al., 2014). Shale beds that are interlayered with more limestone- and sand-rich units have been observed towards the catchment outlet (Jin et al., 2010; Sullivan et al., 2016). The site has gentle slopes, forest cover and very low long-term denudation rates of 0.010 – 0.025 mm yr⁻¹ based on measurements on meteoric beryllium-10 (¹⁰Be; West et al., 2013) and uranium isotope disequilibrium (Ma et al., 2010).

The climate is humid-continental, with a mean annual temperature of 10 °C and mean annual precipitation of 1070 mm (Jin et al., 2010; NADP, 2020).

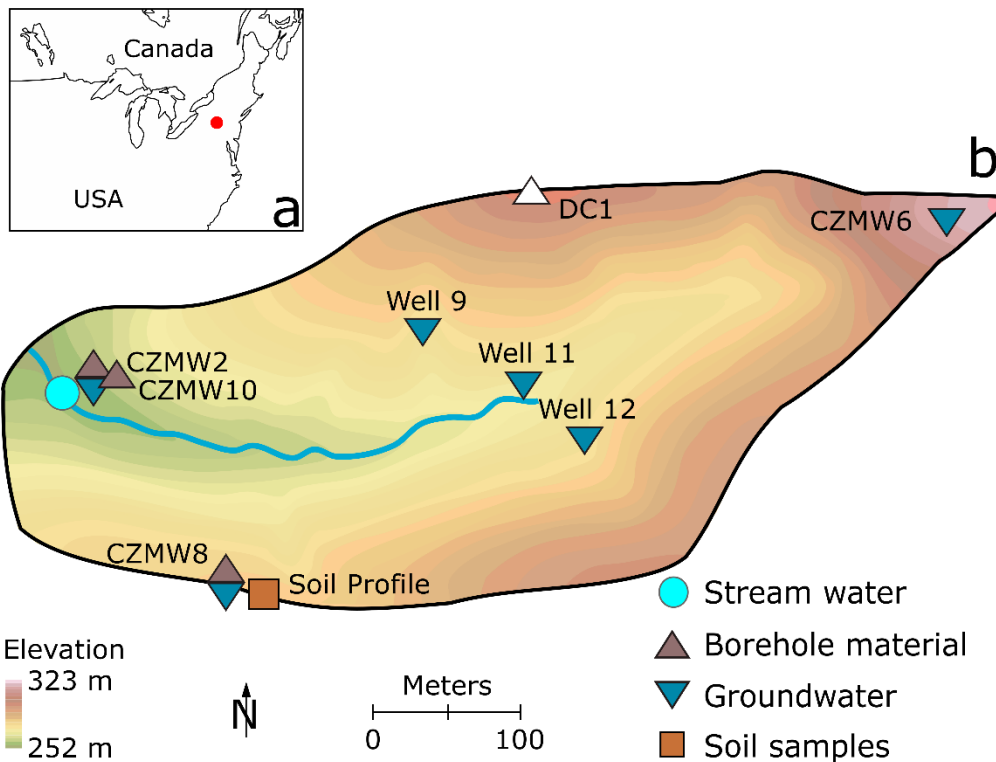


FIGURE 1 (a) The Susquehanna Shale Hills Critical Zone Observatory in central Pennsylvania. (b) The first order Shale Hills catchment and samples analyzed in this study: recovered borehole material (brown triangles) as cuttings (CZMW2, CZMW10) or core (CZMW8); a soil profile (brown square), groundwater samples (blue triangles), and time series stream water samples (June 2018 - June 2019; blue circles). Previously published results from DC1 borehole (white triangle; Jin et al., 2014) are used to help interpretation of the results.

From the early 1800s, the Shale Hills catchment and wider region was logged for charcoal production to support the local iron industry (Herndon et al., 2011; Kraepiel et al., 2015). Today, iron ore smelting and the majority of steel production in the vicinity of Shale Hills has largely stopped. However, several studies report Mn and Pb enrichments in Shale Hills soils derived from coal burning and iron smelting inputs (Herndon and Brantley, 2011; Herndon et al., 2011; Ma et al., 2014). This anthropogenic activity has resulted in acidic (pH ~5.4) and SO_4^{2-} enriched local precipitation (Jin

et al., 2011). A steadily increasing trend in the rain water pH is observed since the early 2000s (NADP, 2020).

Extensive prior research at the SSH-CZO provides insights on carbonate and silicate weathering (Jin et al., 2010, 2011, 2014; Shaughnessy et al., 2020), oxidative weathering of pyrite (Brantley et al., 2013), water-rock interactions (Herndon et al., 2015a; Sullivan et al., 2016), porosity generation and chemical weathering (Gu et al., 2020a, 2020b), and accumulation of metals in top soils (Herndon and Brantley, 2011; Herndon et al., 2011; Ma et al., 2014; Kraepiel et al., 2015). In terms of physical rock degradation, four weathering layers on the Rose Hill shale have been identified: i) soil (hand-augerable material), ii) highly fractured saprock, iii) less fractured saprock and iv) the largely unaltered protolith (Brantley et al., 2013; Jin et al., 2014; Sullivan et al., 2016; Gu et al., 2020a). The term saprock describes fractured bedrock that can reach close to the catchment surface. Previous work attempted a first order estimate of OC_{petro} oxidation, assuming a complete loss of OC from deep samples to the surface (Jin et al., 2014). The authors noted considerable uncertainty due to the low OC concentrations and inputs of carbon from the biosphere.

Materials

Samples were selected from boreholes to assess deeply weathered materials nearer the surface and less weathered samples at depth, using published sulfur concentrations (Brantley et al., 2013; Sullivan et al., 2016;

208 Gu et al., 2020a) to guide where oxidative weathering fronts were located.
209 We focused on two boreholes located in the valley ('CZMW2' and 'CZMW10';
210 Figure 1b). Borehole CMZW2 (sample number; n=11) covers depths
211 between 0.5 m and 16.0 m and documents prominent weathering fronts
212 (Brantley et al., 2013). Deeper samples (7.6 m to 34.9 m) from borehole
213 CZMW10 (n=5) were selected, because they show a wider zone of
214 alteration below the valley (Gu et al., 2020a). The boreholes CZMW2 and
215 CZMW10 were drilled less than 5 m distance from one another, and are
216 considered here as a continuous profile. A third borehole CZMW8, located
217 on the South ridge of the catchment (Figure 1b), has a deeper weathering
218 front, and 8 samples were selected from 0.2 m to 30.6 m depth. Finally, to
219 examine Re in soils, 4 samples from the upper 50 cm deep soil profile
220 previously collected on the south ridge of the catchment (Figure 1b) by
221 Herndon et al. (2011) were selected.

222 Details of soil and borehole sample and data collection methods are
223 provided in previous work (Herndon et al., 2011; Brantley et al., 2013;
224 Sullivan et al., 2016). In summary, the solid samples were air dried,
225 crushed and analyzed for major elements by inductively coupled plasma
226 atomic emission spectroscopy (ICP-AES) and total sulfur (S) by LECO Sulfur
227 Coulometer and LECO Carbon Sulfur Analyzer at Pennsylvania State
228 University. Concentration data have been previously published for
229 boreholes in Brantley et al. (2013), Sullivan et al. (2016) and Gu et al.
230 (2020a).

In this study, 11 stream water samples from the catchment outlet gauging station were collected between June 2018 and June 2019. In August 2018, groundwater samples were collected from wells CZMW2, CMZW8, CZMW6, and wells number 9, 11, and 12 (Figure 1b). Water samples were collected in clean Nalgene bottles, pre-rinsed with the sample water and immediately filtered through 0.22 μm Millipore filters and transferred into acid-cleaned Nalgene bottles (Hilton et al., 2014; Horan et al., 2017). All samples used for trace elements and major cations analyses were acidified to $\text{pH} \sim 2$ with HNO_3 . An un-acidified aliquot was collected in bottles pre-cleaned with demineralized water and filtered stream water for anion analysis, and stored at 4°C in the dark. Archived precipitation samples ($n=4$) collected and stored by similar methods from 2013 (July and October) and 2014 (February and October) were analyzed.

Geochemical analysis

Geochemical analysis of the solid samples from the boreholes included measurements of total organic carbon concentration (TOC), stable OC isotope ratios (reported as $\delta^{13}\text{C}_{\text{OC}}$ relative to VPDB), radiocarbon measurements (^{14}C) of OC, and Re concentrations. Water samples (stream water, groundwater, precipitation) collected for this study were measured for major ion concentrations and trace element Re.

For TOC and $\delta^{13}\text{C}_{\text{OC}}$ measurements, carbonate was removed by weighing ~ 40 mg of a dry sample into a pre-combusted (450°C for 4 hours) silver capsule and adding 2 drops of 1M HCl, followed by drying of the

sample in an oven at 60 °C. To ensure the complete removal of carbonates, each sample was rinsed with 1M HCl three times. The samples were measured on a Sercon ANCA-EA system linked to a Sercon 2022 isotope ratio mass spectrometer (Elemtex, Stable Isotope Analytical Laboratory, Cornwall, UK). Corrections for the procedure and instrumental blanks were applied. The method was validated by measuring the soil standard material NCS-DC73319 for TOC concentration and two international certified synthetic standards, IAEA 600 (caffeine) and IAEA CH3 (cellulose), for $\delta^{13}\text{C}_{\text{OC}}$ values. The standard materials were treated in the same way as the samples. The precision for $\delta^{13}\text{C}_{\text{OC}}$ values was 0.20 ‰ and 0.15 ‰ for IAEA 600 (n=6) and IAEA CH3 (n=6), respectively.

Radiocarbon measurements were made on nine rock samples from the CZMW8 ridgetop borehole. Crushed samples were acid leached (1M HCl) in pre-combusted glassware to remove carbonate minerals. Samples were centrifuged, rinsed with deionized water, and dried in a 60 °C oven at Durham University, Department of Geography. De-carbonated samples were sent to the National Ocean Sciences Acceleration Mass Spectrometry Facility (NOSAMS) at Woods Hole Oceanographic Institution (WHOI) for ^{14}C analysis. A sample aliquot was combusted with CuO and Ag at 850 °C in an evacuated quartz tube. CO_2 was graphitized and measured for radiocarbon following standard procedures via Accelerated Mass Spectroscopy (AMS; McNichol et al., 1994). An aliquot of the CO_2 was used to measure $\delta^{13}\text{C}_{\text{OC}}$ using a VG Prism dual-inlet IRMS. All measurements were corrected for a total procedural blank (combusted quartz sand put through the whole

process) according to conventional radiocarbon reporting standards and reported as Fraction modern ($F^{14}C$) as per Stuiver and Polach (1977).

Rhenium concentrations in the borehole solids were measured following complete acid digestion ($HF+HNO_3$, followed by aqua regia) and anion exchange column chemistry as per methods of Dellinger et al. (2020). The Re solutions were measured on a Thermo Scientific Neptune Plus at Durham University, Department of Earth Sciences. Standard reference materials were digested in each batch to validate the method; a marine sediment (MAG-1), basalt (BHVO-2, BCR-2), and serpentinite (UB-N), which returned values for this study in close agreement; <15% with previously published data (Meisel and Moser, 2004; Jochum et al., 2016) and <10% with long-term in-house reproducibility (Dellinger et al., 2020).

Major ions (Cl^- , SO_4^{2-} , Na^+ , K^+ , Ca^{2+} , Mg^{2+}) in water samples were determined by ion chromatography (Dionex ICS 3000, Durham University, Department of Geography), validated by a certified river water reference standard material (Sangamon-03). The difference between our measurements and certified reference material values for all major elements was <5% ($n=3$). The analytical precision determined by running replicates on selected samples was <3% ($n=5$) for all reported major ions.

Concentrations of dissolved Re were determined by a direct calibration method (Horan, 2018) on Agilent Technologies 7900 inductively coupled plasma mass spectrometer (ICP-MS) at Durham University, Department of Geography. The detection limit defined as 3 standard deviations of the replicate measurements of a blank solution was 0.01 ppt for Re. Repeated

measurements of the river water standard sample SLRS-5 for Re are 64.6±6.1 ppt (±1SD, n=6) and 10- and 100-times dilutions are 6.2±0.7 ppt (±1SD, n=6) and 0.63±0.1 ppt (±1SD, n=6), respectively. These are in agreement with the long-term in house reproducibility, that is SLRS-5=63.0±3.5 ppt (±1SD, n=24), SLRS-5×10=6.2±0.3 ppt (±1SD, n=21), and SLRS-5×100=0.61±0.10 ppt (±1SD, n=35), and with Re concentrations for SLRS-5 reported in literature: 66±12 ppt (Yeghicheyan et al., 2013).

Calculation of mass transfer coefficient (τ)

In the borehole sediments, a mass transfer coefficient (τ) was calculated to characterize the mobility of S, TOC, and Re during weathering. The coefficient τ describes a gain or loss of an element relative to the parent material by applying Equation 1 (Brimhall and Dietrich, 1987; Anderson et al., 2002).

$$\tau_{i,s} = \frac{C_{j,s} C_{i,p}}{C_{j,p} C_{i,s}} - 1 \quad (1)$$

Where C is the concentration of the mobile element (j) or immobile element (i) in the protolith (p) or soil/saprock (s). The approach assumes that composition of the protolith is relatively homogeneous, with mean composition and variability that can be defined, and that the species (i) is immobile through the weathering profile. A negative τ value describes a relative depletion of an element compared to the immobile element in the

parent material. We use Zr as the immobile element following the approach of Kraepiel et al. (2015).

Results

Here, a summary of previous results is provided before outlining new measurements of TOC, $\delta^{13}\text{C}_{\text{OC}}$, ^{14}C and Re concentrations (Figure 2). Mobility during oxidative weathering is assessed with mass transfer coefficients for S, TOC and Re (Figure 3). New measurements of major ion and Re concentrations in stream water, groundwater and precipitation are given to constrain Re cycling in the near surface environment.

Published sulfur concentrations in borehole materials

The depletion of S in the borehole samples provides insight on oxidative weathering of pyrite at Shale Hills because almost all sulfur in the parent rock is present in pyrite (Brantley et al., 2013; Sullivan et al., 2016; Gu et al., 2020a). In the valley (CZMW2, CZMW10), the S concentrations are low from the surface through the weathered saprock to depths of ~ 6.5 m, with a mean S of 0.005 ± 0.002 wt.% ($n=17$, $\pm 1\text{SD}$; Brantley et al., 2013; Gu et al., 2020a). A wide (~ 15 m) pyrite depletion zone, with continuous increase in S concentration is observed between ~ 6.5 m and ~ 21.4 m, with a mean S of 0.08 ± 0.03 wt.% ($n=26$, $\pm 1\text{SD}$). The highest S concentrations are measured below ~ 21.4 m, with a mean S of 0.15 ± 0.04 wt.% ($n=17$, $\pm 1\text{SD}$) in the protolith. On the ridge, the weathered saprock extends deeper, to ~ 15.4 m and has mean S of 0.02 ± 0.03 wt.% ($n=10$, $\pm 1\text{SD}$;

Sullivan et al., 2016). Beneath the S-depleted layers, a sharp increase in S concentrations from below detection limit (~ 0.002) to 0.14 wt.% is observed between 15.4 m and 16.4 m depth. This increase is consistent with decrease of saprock porosity and fracture density (Sullivan et al., 2016; Gu et al., 2020a).

TOC, $\delta^{13}\text{C}_{\text{OC}}$ and ^{14}C in borehole materials

The TOC concentrations are highest in the surface soil, with 0.14 wt.% and 0.32 wt.% measured in the valley (down to ~ 1 m; CZMW2). Lower TOC concentrations were found in the upper part of the weathered saprock (down to ~ 6.5 m, i.e. above the pyrite depletion zone; CZMW2), with TOC values of 0.06 wt.% and 0.07 wt.%. At a depth of ~ 8.4 m the TOC concentrations are the lowest at 0.03 wt.% and they stay low until ~ 16 m depth, with a mean value of 0.04 ± 0.01 wt.% ($n=6$, $\pm 1\text{SD}$, CZMW2). On the ridge, the TOC concentrations are also the highest in the surface soil at 0.41 wt.% (down to ~ 0.3 m; CZMW8). The TOC concentrations drop in the weathered saprock (~ 0.9 to ~ 12.4 m) to span a range of values between 0.09 wt.% (the top most sample at 0.9 m) to 0.05 wt.% at ~ 12.4 m. At ~ 15.4 m depth the lowest TOC concentration is measured at 0.03 wt.%, which gradually increases in the protolith to a value of 0.06 wt.% at 30.5 m depth (CZMW8). The TOC values are similar to those reported by Jin et al. (2010, 2014) sampled in borehole DC1, located on the North ridge of the Shale Hills catchment (Figure 1b).

The stable carbon isotopic composition of the organic carbon ($\delta^{13}\text{C}_{\text{OC}}$) varies by up to ~ 2 ‰, but does not show any systematic variation between the soil, saprock and protolith samples, in both boreholes CZMW2 (-26.3 ‰ to -24.4 ‰) and CZMW8 (-27.0 ‰ to -26.2 ‰). These values are similar to $\delta^{13}\text{C}_{\text{OC}}$ values of soils (-25.8 ‰ to -25.3 ‰) and protolith samples (-27.1 ‰ to -25.9 ‰) previously published for Shale Hills in Jin et al. (2014).

The radiocarbon activity, reported as Fraction modern ($F^{14}\text{C}$), in the CZMW8 ridgetop borehole varies between 0.91 ± 0.005 near the surface, to 0.24 ± 0.003 in the saprock, at ~ 15.4 m depth. The high $F^{14}\text{C}$ measured in the top soil is consistent with organic matter dominated by the modern biosphere, resulting in a $F^{14}\text{C}$ value close to 1 (Trumbore, 2009). Within the saprock, lower $F^{14}\text{C}$ values are consistent with some input of OC_{petro} from the Silurian Rose Hill formation that was deposited ~ 443 to 416 million years ago ($F^{14}\text{C}$ value=0). However, the presence of ^{14}C , with $F^{14}\text{C}$ between 0.26 ± 0.003 and 0.32 ± 0.003 in the deep profile, suggests potential aging of biospheric OC and/or another source of ^{14}C -enriched C in the deepest samples, as discussed in Section 4.1.

Re concentration in borehole materials and surface soils

The protolith samples (below ~ 21.4 m) under the valley (CZMW2 and CZMW10) have the highest Re concentrations, ranging between 0.10 ppb and 0.42 ppb. These are similar to Re concentrations for the protolith under the ridge (below ~ 15.4 m in CZMW8) of 0.11 ppb to 0.23 ppb. The Re

concentrations in the Shale Hills protolith are more than 100-times lower than those measured in black shale weathering profiles from the US (Jaffe et al. 2002) and Nepal (Pierson-Wickmann et al., 2002), but similar to those from river bed material in the western Southern Alps of New Zealand (mean Re = 0.12 ± 0.02 ppb), which is also derived from an OC-poor (TOC $\sim 0.13\%$) rock (Horan et al., 2017).

In the valley, Re is depleted in the weathered saprock from ~ 0.9 m to ~ 6.5 m to between 0.02 ppb and 0.03 ppb. Similar Re concentrations are measured in saprock under the ridge. The pattern of Re depletion is spatially consistent with the S depletion (Brantley et al., 2013; Sullivan et al., 2016; Gu et al., 2020b) and is consistent with weathering profiles developed on black shales (Jaffe et al., 2002; Pierson-Wickmann et al., 2002). A slight increase in Re concentration towards the surface soil is measured in both boreholes to ~ 0.06 ppb. In the ridgetop soil profile (Figure 2f), the highest Re concentration of 0.12 ppb is measured in the top soil (2.5 cm), which decreases to 0.01 ppb at 42.5 cm depth.

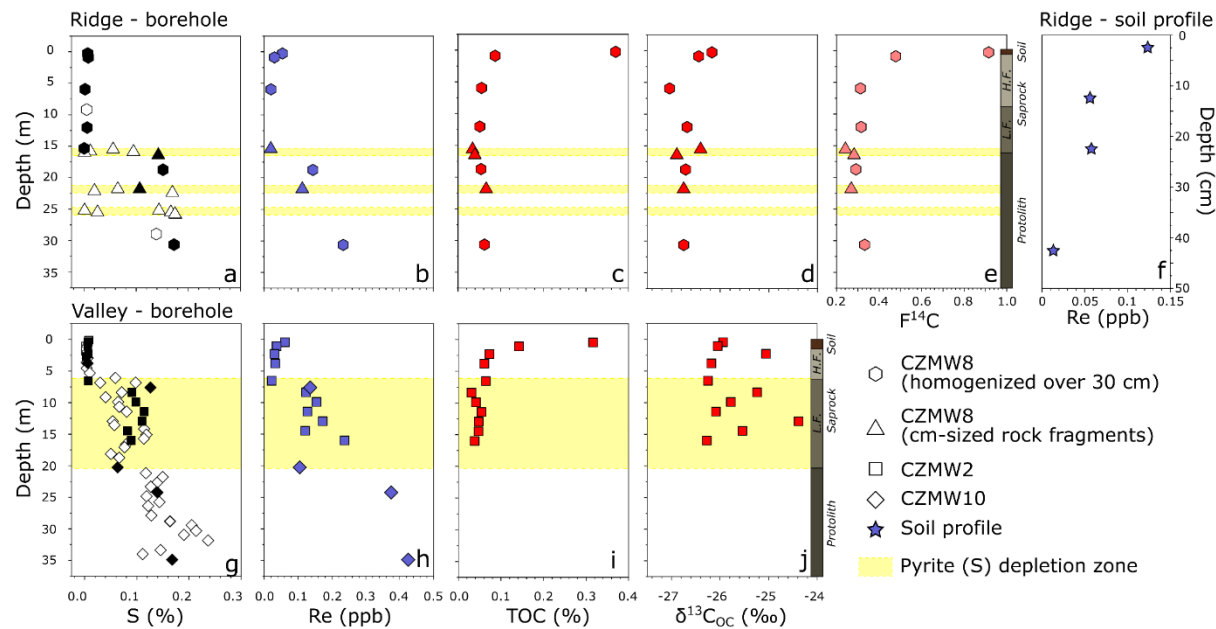


FIGURE 2 Geochemical profiles for boreholes CZMW8 (southern ridge) and CZMW2, CZMW10 (valley). (a) Previously published measurements of sulfur (S) concentrations from boreholes CZMW2 and CZMW10 in Brantley et al. (2013) and Gu et al. (2020a) and from the borehole CZMW8 in Sullivan et al. (2016) and Gu et al. (2020a). Samples were selected (black symbols in figures (a) and (g) and analyzed for rhenium (b) and (h), total organic carbon (c) and (i), stable carbon isotope of organic carbon (d) and (j), and radiocarbon (Fraction modern, e). From the borehole CZMW8 two types of samples were collected: bulk core material homogenized over 30 cm depth (hexagons) and cm-sized rock fragments (triangles). Bar to the right side of plots (e) and (j) show approx. depths of changes in structure due to chemical and physical degradation of the protolith (Sullivan et al., 2016). H.F. stands for highly fractured saprock and L.F. stands for less fractured saprock. The yellow shading on all plots show depth intervals where pyrite depletion was detected (Brantley et al., 2013; Sullivan et al., 2016; Gu et al., 2020a). The uppermost white band for each borehole represents the bulk oxidation zone because almost no pyrite remains unoxidized at

419 shallower depths (lower yellow bands are fracture sets as described by (Gu et al., 2020a). Figure (f) shows Re
420 concentrations from a soil profile sampled next to CZMW8.

421 **TABLE 1** Published sulfur, zirconium and titanium concentrations alongside new measurements of total organic
422 carbon (TOC), stable carbon isotope of organic carbon ($\delta^{13}\text{C}_{\text{OC}}$), radiocarbon activity ($F^{14}\text{C}$), and rhenium (Re) in the
423 studied borehole profiles and the topsoil profile. Classification of material type is based on previous work by Sullivan
424 et al., 2016 (1), Brantley et al., 2013 (2) Gu et al, 2020a (3) and Herndon et al., 2011 (4). Radiocarbon activities
425 of the biospheric OC input used in the two end-member mixing model applied for determination of OC_{petro}
426 concentrations are discussed in section 4.1 ($F^{14}\text{C} = 1.1 - 0.9$ for samples labelled * and $F^{14}\text{C} = 0.9 - 0.5$ for samples
427 labelled **).
428

Borehole	Sample ID	Depth (m)	Material type	$\delta^{13}\text{C}$ ‰	TOC (%)	$F^{14}\text{C}$	OC_{petro} (%)	$\text{OC}_{\text{petro}} + 2\sigma$	$\text{OC}_{\text{petro}} - 2\sigma$	Re (ppb)	S (%)	Zr (ppb)	Ti (%)	S, Ti (%), Zr (ppb) and material type ref.
CZMW8	SSH0001SI	-0.27	Soil	-26.2	0.37	0.91 ± 0.005	0.03*	0.057	0.001	0.05	0.006	186	0.62	1
	SSH0001SJ	-0.88	Saprock	-26.4	0.09	0.47 ± 0.003	0.03**	0.037	0.007	0.03	0.007	158	0.59	1
	SSH0001SL	-5.94	Saprock	-27.0	0.06	0.30 ± 0.003	0.03**	0.032	0.020	0.02	0.001	163	0.62	1
	SSH0001T5	-12.04	Saprock	-26.7	0.05	0.31 ± 0.003	0.02**	0.029	0.018	-	0.005	152	0.59	1
	SSH0001TH	-15.36	Saprock	-26.4	0.03	0.24 ± 0.003	0.02**	0.021	0.015	0.02	0.002	141	0.59	1
	SSH0001TP	-16.40	Protolith	-26.9	0.04	0.27 ± 0.003	0.02**	0.023	0.016	-	0.142	145	0.63	1
	SSH0001TX	-18.75	Protolith	-26.7	0.05	0.28 ± 0.003	0.03**	0.032	0.021	0.14	0.122	149	0.58	1
	SSH0001O7	-21.49	Protolith	-26.8	0.07	0.26 ± 0.003	0.04**	0.041	0.028	0.11	0.100	142	0.61	1
Parent	SSH0001V4	-30.36	Protolith	-26.8	0.06	0.32 ± 0.003	0.03**	0.034	0.020	0.23	0.172	138	0.61	1
CZMW2	SSH000SWY	-0.46	Soil	-25.9	0.32	-	-	-	-	0.06	0.006	225	0.55	2
	SSH000SX0	-1.07	Soil	-26.0	0.14	-	-	-	-	0.04	0.006	230	0.58	2
	SSH0001KN	-2.29	Saprock	-25.1	0.07	-	-	-	-	0.03	0.007	175	0.53	2
	SSH000SX5	-3.81	Saprock	-26.2	0.06	-	-	-	-	0.03	0.006	245	0.58	2
	SSH000SX6	-6.55	Saprock	-26.2	0.06	-	-	-	-	0.02	0.007	185	0.47	2
	SSH000SX8	-8.38	Saprock	-25.2	0.03	-	-	-	-	0.12	0.091	160	0.58	2
	SSH000SX9	-9.91	Protolith	-25.8	0.04	-	-	-	-	0.15	0.098	165	0.58	2
	SSH000SXA	-11.43	Protolith	-26.1	0.05	-	-	-	-	0.13	0.114	140	0.58	2
	SSH000SXB	-12.96	Protolith	-24.4	0.05	-	-	-	-	0.17	0.110	175	0.57	2
	SSH000SXC	-14.48	Protolith	-25.5	0.05	-	-	-	-	0.12	0.082	165	0.59	2
	SSH000SXD	-16.01	Protolith	-26.3	0.04	-	-	-	-	0.24	0.089	315	0.64	2
CZMW10	SSH0003DG	-7.62	Saprock	-	-	-	-	-	-	0.14	0.126	166	0.59	3
	SSH0003DV	-20.27	Protolith	-	-	-	-	-	-	0.10	0.063	156	0.56	3
	SSH0003EO	-24.23	Protolith	-	-	-	-	-	-	0.37	0.140	239	0.53	3

Parent	SSH0003EC	-34.90	<i>Protolith</i>	-	-	-	-	-	-	0.42	0.168	185	0.62	3
		Depth interval (cm)												
Soil profile	SSH00000R	0-5	<i>Soil</i>							0.12		250	-	4
	SSH00000R	10-15	<i>Soil</i>							0.05		275	-	4
	SSH00000R	20-30	<i>Soil</i>							0.06		210	-	4
	SSH00000R	40-50	<i>Soil</i>							0.01		170	-	4

430 Mass transfer coefficient

431 To assess the loss or gain of elements, the composition of the parent
432 material must be characterized. At SSH-CZO, this is not straightforward,
433 due to potential heterogeneity of the parent material over the deep
434 weathering zone (Brantley et al., 2013b; Gu et al., 2020b) and appearance
435 of deep fractures that sometimes show localized zones of weathering
436 depletion (Gu et al., 2020a). Previous studies have used an average over
437 several samples to characterize the parent material, and the standard
438 deviation to assess potential variability on tau values (Brantley et al., 2013;
439 Sullivan et al., 2016; Gu et al., 2020b). Due to the limited number of Re
440 and ^{14}C measurements in the protolith (Figure 2b and e), we here use the
441 deepest sample and assume that the variability in the protolith for those
442 elements is similar to that measured for S (relative standard deviation).

443 The calculated tau values for S (Figure 3a and d), reveal nearly
444 complete loss of S from the top 6.5 m under the valley ($\tau_{Zr,S}=-0.95\pm0.08$)
445 and from the top 15.4 m under the ridge ($\tau_{Zr,S}=-0.89\pm0.19$), agreeing with
446 previous results (Brantley et al., 2013; Sullivan et al., 2016; Gu et al.,
447 2020a). The tau values for Re are less negative than S, but still show
448 substantial depletion in the valley ($\tau_{Zr,Re}=-0.84$ to -0.93 ; Figure 3f) and
449 under the ridge ($\tau_{Zr,Re}=-0.77$ to -0.92 ; Figure 3c). Due to a lower number
450 of samples analyzed for Re, the comparison between S and Re is not
451 straightforward. Nonetheless, depletion of Re and S is coherent at 15.4 m
452 and 6.5 m depth under the ridge and valley, respectively (Figure 3).

453 There is TOC accumulation in the top meter of the profile under the
454 valley ($\tau_{Zr,TOC}=+5.9$ and $+2.0$; Figure 3e) and the ridge ($\tau_{Zr,TOC}=+3.6$;
455 Figure 3b). For the ridge profile, TOC shows a decrease in tau between 21.4
456 and 15.4 m, with a minimum value of $\tau_{Zr,TOC}=-0.55$ (Figure 3b), tracking Re
457 loss. A less pronounced depletion zone is observed in the borehole under
458 the valley, with the deepest sample being the most depleted showing a
459 $\tau_{Zr,TOC}$ of -0.41 .

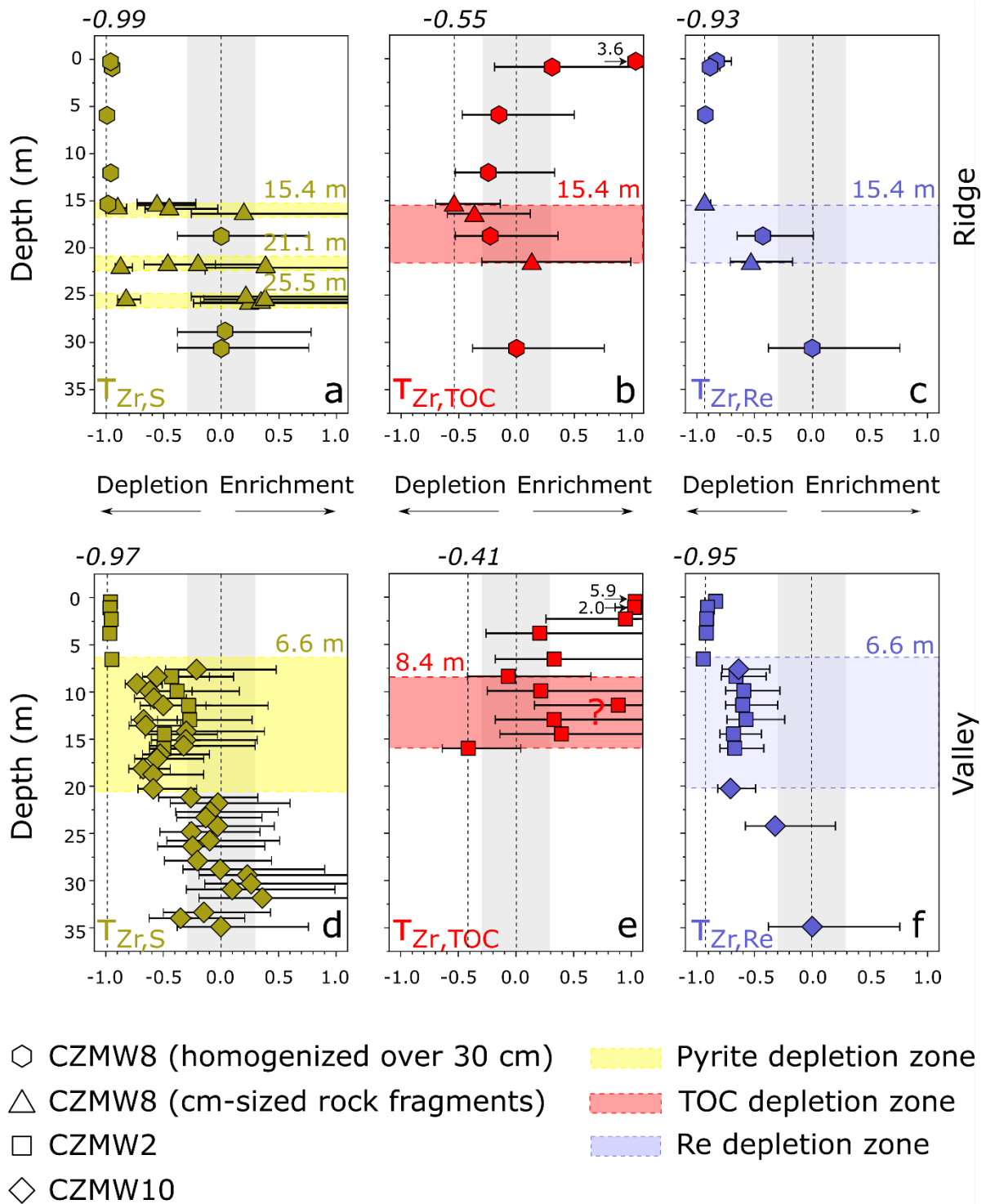


FIGURE 3 Mass transfer coefficient profiles for boreholes CZMW8 (southern ridge) and CZMW2, CZMW10 (valley). Parent composition was determined from the concentration measured on the deepest protolith sample in the CZMW8 and CZMW10. Zirconium (Zr) was used as an immobile element. The error bars show variation of the parent material for S (33%) and Zr (18%). For TOC and Re it is assumed that the variability in the parent material is similar to the S (~30%). Shaded grey zone represents one SD of uncertainty due to variable parent composition within the catchment(a)

$\tau_{Zr,S}$ profile from the ridge (CZMW8). Data and interpretation is from Gu et al. (2020a). (b) $\tau_{Zr,TOC}$ profile from the ridge (CZMW8). (c) $\tau_{Zr,Re}$ profile from the ridge (CZMW8). (d) $\tau_{Zr,S}$ profile from the valley (CZMW2, CZMW10). Data and interpretation is from (Brantley et al., 2013; Gu et al., 2020a). (e) $\tau_{Zr,TOC}$ profile from the valley. (f) $\tau_{Zr,Re}$ profile from the valley.

Stream water chemistry

The stream water is dominated by Ca^{2+} , with a mean value of $205 \pm 83 \mu\text{mol l}^{-1}$ (all stream waters: $n=11$, $\pm 1\text{SD}$, unless otherwise stated). Mg^{2+} , Na^{+} , and SO_4^{2-} concentrations are lower, with a mean value of $88 \pm 21 \mu\text{mol l}^{-1}$, $28 \pm 5.6 \mu\text{mol l}^{-1}$ and $80 \pm 6.6 \mu\text{mol l}^{-1}$, respectively. These measurements are consistent with data collected at SSH-CZO between 2006 and 2011 (Herndon et al., 2015a). Dissolved Re concentrations show less variation than the major ions, with values between 3.8 to 5.5 pmol l^{-1} , and a mean of $4.3 \pm 0.6 \text{ pmol l}^{-1}$, which is towards the lower end of published Re values for river water (Miller et al., 2011). During the sampling period (2018-2019), average daily water discharge was 2.27 l s^{-1} , which is slightly higher than the long term mean (2008-2015) of 1.07 l s^{-1} (Shi and Xiao, 2019).

Groundwater and precipitation chemistry

In agreement with previous work (Jin et al., 2014), groundwater is more concentrated in Na^{+} , Ca^{2+} , and Mg^{2+} ions compared to stream water (Table 2). In contrast, the mean SO_4^{2-} concentration in groundwater of $76 \pm 30 \mu\text{mol l}^{-1}$, is similar to values measured in the stream. Rhenium concentrations in groundwater samples show a larger range, from

495 1.3 pmol l⁻¹ to 10.0 pmol l⁻¹. The highest Re concentrations were measured
496 in two wells located along the stream channel: 6.3 pmol l⁻¹ and 10.0 pmol l⁻¹
497 for CZMW2 and Well 11 (Figure 1b). In these wells, water table was close
498 to the land surface, indicating a groundwater contact with surface soils.

499 The Re concentration in precipitation ranged between 0.43 pmol l⁻¹
500 and 2.95 pmol l⁻¹, with a mean value of 1.27 ± 1.14 pmol l⁻¹ (n=4; ±1SD)
501 close to those measured in stream water. This is in contrast to very low
502 dissolved Re concentrations of <0.2 pmol l⁻¹ in rain from New Zealand
503 (Horan et al., 2017), the European Alps (Hilton et al., 2021) and the coastal
504 range California (Ghazi et al., 2022), but is similar to the values reported
505 for rainwater from Falmouth, Massachusetts, on the East coast of the US,
506 which reach 5.9 pmol l⁻¹ (Miller et al., 2011).

507 **TABLE 2.** Dissolved load chemistry on stream water, groundwater and precipitation samples. Major ions on the
508 precipitation samples are from NADP Program Office (2020) database obtained in the same week as the samples
509 analyzed for Re.
510

Sample Name	Sampling Date	Sample type	Location	Instantaneous discharge l s ⁻¹	Cl ⁻ μmol	SO ₄ ²⁻ μmol	Na ⁺ μmol	K ⁺ μmol	Mg ²⁺ μmol	Ca ²⁺ μmol	Re pmol
SH18-04	19/08/2018	Stream water	Gauging station	0.3	21	77	30	28	101	242	5.16
SH 20-06-18	20/06/2018	Stream water	Gauging station	20.4	23	83	40	29	131	332	4.09
SH 03-08-18	03/08/2018	Stream water	Gauging station	1.2	16	65	20	26	53	57	5.51
S19-1	06/02/2019	Stream water	Gauging station	2.8	20	76	25	25	69	101	4.17
S19-2	27/02/2019	Stream water	Gauging station	1.5	17	83	25	22	79	146	3.81
S19-3	13/03/2019	Stream water	Gauging station	4.2	18	86	23	20	74	292	4.67
S19-4	31/03/2019	Stream water	Gauging station	0.6	18	89	29	22	97	243	4.11
S19-5	17/04/2019	Stream water	Gauging station	3.1	16	81	23	23	73	149	3.76
S19-6	01/05/2019	Stream water	Gauging station	0.6	19	87	33	25	104	256	4.22
S19-7	23/05/2019	Stream water	Gauging station	1.0	18	81	28	25	94	218	3.99
S19-8	03/06/2019	Stream water	Gauging station	1.0	18	80	28	25	91	212	3.91
SH18-02	19/08/2018	Groundwater	Well nr. 11	-	28	80	40	29	86	69	10.00
SH18-05	19/08/2018	Groundwater	CZMW2	-	29	132	296	17	214	1028	6.26
SH18-10	20/08/2018	Groundwater	Well nr. 09	-	25	78	43	35	99	97	4.93
SH18-12	20/08/2018	Groundwater	Well nr. 12	-	37	47	162	37	504	330	1.27
SH18-11	20/08/2018	Groundwater	CZMW8	-	20	64	31	25	49	39	3.55
SH18-13	20/08/2018	Groundwater	CZMW6	-	23	54	29	36	270	257	4.51
Rain 10/07/13	07/10/2013	Rain	-	-	1.3	4.5	0.9	2.6	0.7	1.1	0.43
Rain 2014/10/23	23/10/2014	Rain	-	-	1.0	19.2	0.2	0.2	0.5	1.9	2.95
Rain 7/1/13	01/07/2013	Rain	-	-	1.0	7.8	0.3	0.3	0.4	1.6	1.02
Snow 02/07/14	07/02/2014	Snow	-	-	2.1	3.9	0.7	0.2	0.2	0.7	0.70

512 Discussion

513 The borehole materials from Shale Hills display notable Re loss, with a
514 depletion front which broadly coincides with that of pyrite (S) loss.
515 Assessing the location of the OC_{petro} reaction front using only %TOC is
516 challenging, with clear evidence for modern OC inputs in the near surface
517 samples. Here we use radiocarbon and attempt to quantify OC_{petro} content
518 with an aim to determine the long-term Re and OC_{petro} oxidation rates.
519 Finally, we discuss the enrichment of Re in the near surface soils, stream
520 water and precipitation, in the context of anthropogenic inputs of Re in a
521 low denudation setting.

522 Evidence for OC_{petro} loss during weathering

523 The borehole profiles of TOC and $\tau_{Zr,TOC}$ contain information on OC_{petro} loss,
524 and show a depletion of TOC coincident with the Re and S reaction fronts
525 (Figure 3). However, the TOC concentration in the Rose Hill shale is low
526 (Table 1, Jin et al., 2014), and C inputs from organic matter of the modern
527 biosphere or other non-petrogenic sources need to be assessed carefully.
528 The $\delta^{13}C_{OC}$ values are not helpful to distinguish source, showing no
529 systematic variation between the soil, saprock, and protolith (Figure 2d).

530 Instead, we use the radiocarbon activity ($F^{14}C$) of the bulk organic
531 matter in the ridgetop borehole (CZMW8) (Figure 2e). However, we find no
532 fully ^{14}C -depleted sample, contrasting with other sedimentary rock
533 weathering profiles where OC content of the rock is >1% (Petsch, 2014;

Hilton et al., 2021). This requires a source of OC at depth that contains radiocarbon. The most ^{14}C -enriched source in the catchment is recent organic matter formed by photosynthesis ($F^{14}\text{C} \sim 1$). The sample at 0.23 m depth, with a $F^{14}\text{C}=0.91$, could be mostly explained by input from modern OC_{bio} . To explain the input of ^{14}C over the deep weathering profile studied here, we discuss three possibilities: i) aging of plant derived particulate matter, ii) supply and aging of dissolved OC (DOC), and/or iii) chemotrophic fixation of DIC at depth.

The aging of plant-derived organic matter in mineral soil horizons lowers $F^{14}\text{C}$ (e.g., $F^{14}\text{C}$ value of 0.7 corresponds to 2,865 radiocarbon years). This could fully explain the surface most sample ($^{14}\text{C}=0.91$) and partly explain the ^{14}C -depletion of the sample at 0.88 m depth ($F^{14}\text{C}=0.47$). Large particles of OC from the biosphere may be transported deeper into the profile during drilling process. However, other pathways, such as percolating dissolved OC (DOC) downwards from the surface via flow pathways through the saprock (Marin-Spiotta et al., 2011), or colloidal transport of OC (Yan et al., 2018; Kim et al., 2018) are also possible. A final mechanism to deliver ^{14}C -rich OC to depth could be via the dissolved inorganic carbon (DIC) pool via chemotrophic production of organic matter. The DIC pool may have $F^{14}\text{C}$ between 0.5 and 1.0 reflecting acid hydrolysis of carbonate and silicate minerals from a mixture of atmospheric CO_2 and carbonate mineral weathering (Jin et al., 2014). This could be incorporated into microbial biomass under water-saturated conditions (i.e. low O_2) via SO_4^{2-} reduction (Schwab et al., 2019). Distinguishing these pathways is not

possible here, but remains an important avenue for future research if these processes can store significant amounts of recent carbon at depth in weathered rocks.

To quantify OC_{petro} using ^{14}C we consider all of these possible pathways for ^{14}C addition. We assume that the bulk OC pool is a mixture between OC_{petro} ($F^{14}\text{C}=0$) and an ^{14}C -enriched pool (Blair et al., 2003; Galy et al., 2008; Hemingway et al., 2018). In the near surface, we assume that the $F^{14}\text{C}$ values of the enriched pool vary between 1.1 (potential bomb ^{14}C inputs) to 0.9 (potential aged particulate or DOC). Deeper in the profile, we consider C with $F^{14}\text{C}$ values between 0.9 (potential aged DOC) to 0.5 (chemotrophic C input from DIC). As per Hilton et al. (2021) this range is used for each sample with a Monte Carlo simulation (1,000-times per sample) to return modelled OC_{petro} concentration values, reported as the 50% (median), $+2\sigma$ and -2σ , together including 95% of the predicted OC_{petro} values (Table 1, Figure 4a).

The least well constrained OC_{petro} contents are from the most surface sample, with modelled values between 0.057% and 0.001%. These correspond to a $\tau_{\text{Zr},OC_{\text{petro}}}$ value varying between +0.46 and -0.97 (Figure 4b). The uncertainty comes from the modest ^{14}C -depletion, which could be entirely explained by biospheric OC aging (i.e., negligible OC_{petro} inputs), and because the OC_{petro} contents are low compared to the %TOC values (Figure 2c). It is likely that the approach here over-estimates OC_{petro} in the upper most sample. With increasing depth OC_{petro} concentration is better constrained. Between 21.5 m and 15.4 m there is a decrease in

modelled OC_{petro} , from 0.04% to 0.02% (Figure 4a). The corresponding $\tau_{\text{Zr}, OC_{\text{petro}}}$ decreases from +0.22 to -0.36 (Figure 4b).

Despite the very low OC_{petro} contents of the protolith at Shale Hills, the challenges of applying ^{14}C as a proxy for OC_{petro} input and limited number of samples, there is evidence for an OC_{petro} reaction front. Admittedly, there may be variability in the OC_{petro} content of the bedrock, but this variation would have to be coincident with the depths at which S and Re are depleted. Future work could unpack OC inputs and C cycle processes using the ramped pyrolysis oxidation (RPO) coupled to radiocarbon technique, to isolate OC with different thermal reactivity (Hemingway et al., 2017; Grant et al., 2019). Here, we turn to the loss of Re as an alternative approach to constrain oxidative weathering processes and fluxes at Shale Hills.

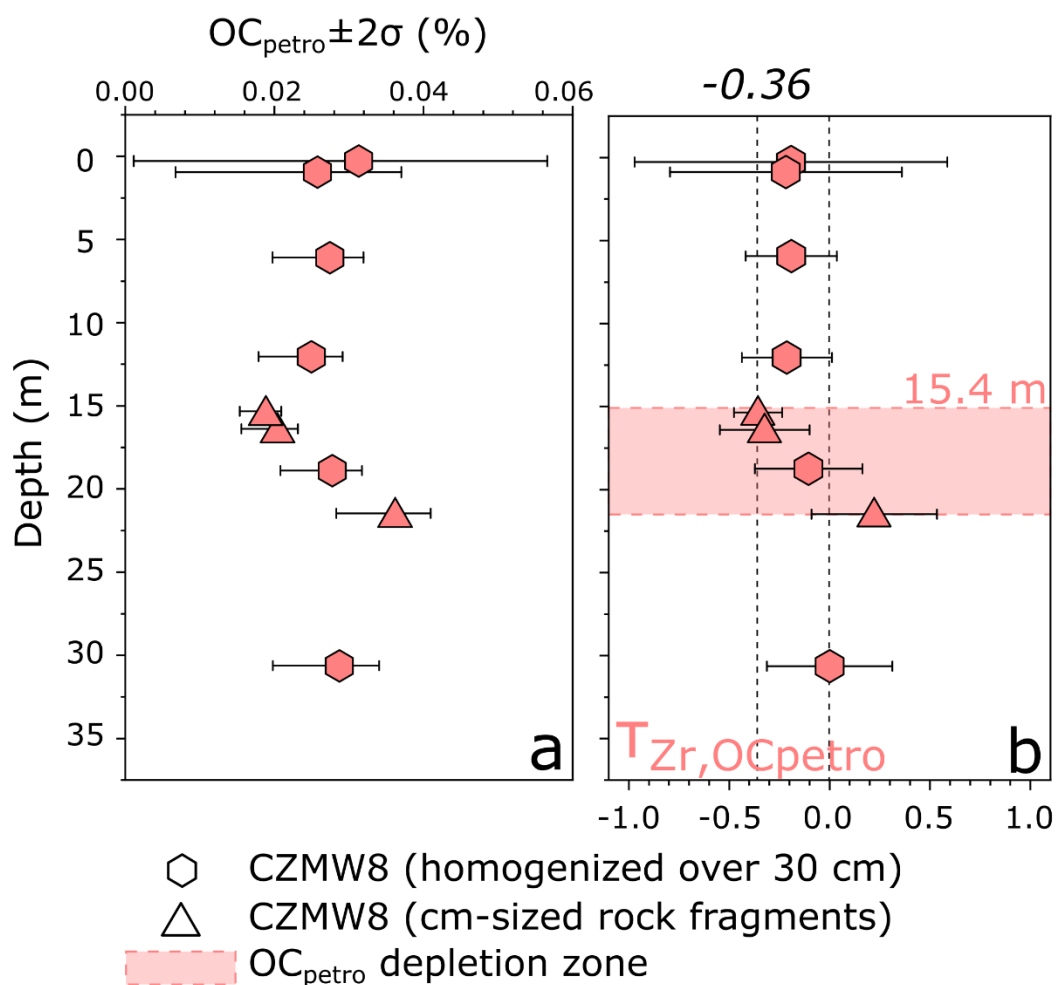


FIGURE 4 (a) Modelled rock organic carbon concentrations (OC_{petro}) determined from radiocarbon measurements on the samples from the ridge borehole (CZMW8). (b) Mass transfer coefficients plotted versus depth to track mobility of OC_{petro} . Parent composition was determined from the concentration measured on the deepest protolith sample in CZMW8. Zirconium (Zr) was used as an immobile element.

Source of Re in borehole sediments

The application of Re as a proxy for OC_{petro} oxidation rates is built on an assumption that OC_{petro} represents a major source of Re in the weathered lithology (Dalai et al., 2002; Hilton et al., 2014). Here, we use the ratio of Re to Na and S to quantify the role of sulfide- and silicate-derived Re (as per Horan et al., 2019 and Hilton et al., 2021). In general, Re

concentrations of silicate and sulfide minerals are low, resulting in low Re/Na ratios for silicates, and low Re/S ratios for sulfides (Peucker-Ehrenbrink and Hannigan, 2000; Dalai et al., 2002; Miller et al., 2011). In contrast, Re enrichment associated with OC can increase Re/Na and Re/S ratios (Das et al., 2012). Horan et al. (2019) proposes a Re/S ratio of 6.0×10^{-4} pmol/ μ mol; however, recent work showed that Re/S ratio can be as low as 9.1×10^{-5} in a sedimentary, shale environment (Ogrič, 2021). The end-member composition for silicates (Re/Na) is between 2.4×10^{-4} and 2.2×10^{-3} pmol/ μ mol (Dalai et al., 2002).

The three-component mixing domain suggests that in the deeper samples, Re is largely associated with OC_{petro} (Figure 5), having a range of relative inputs between 77% and 93%, and a mean value of $83 \pm 6\%$ (± 1 SD n=13). Moving towards the surface, an increase in Re/S and decrease in Re/Na ratios are seen in weathered samples (Figure 5). The increase in Re/S ratio though weathering implies preferential loss of S relative to Re. The decrease in Re/Na ratio suggests that Re associated with OC_{petro} is lost during weathering, consistent with evidence for OC_{petro} loss (Figure 4). These observations suggest that, despite the low %TOC of the rocks, the majority of Re is associated with OC_{petro} at depth, and that Re loss results in a residual that becomes more dominated by silicate-derived Re. Rhenium isotope measurements from a black shale weathering profile were explained invoking similar behavior (Miller et al., 2015).

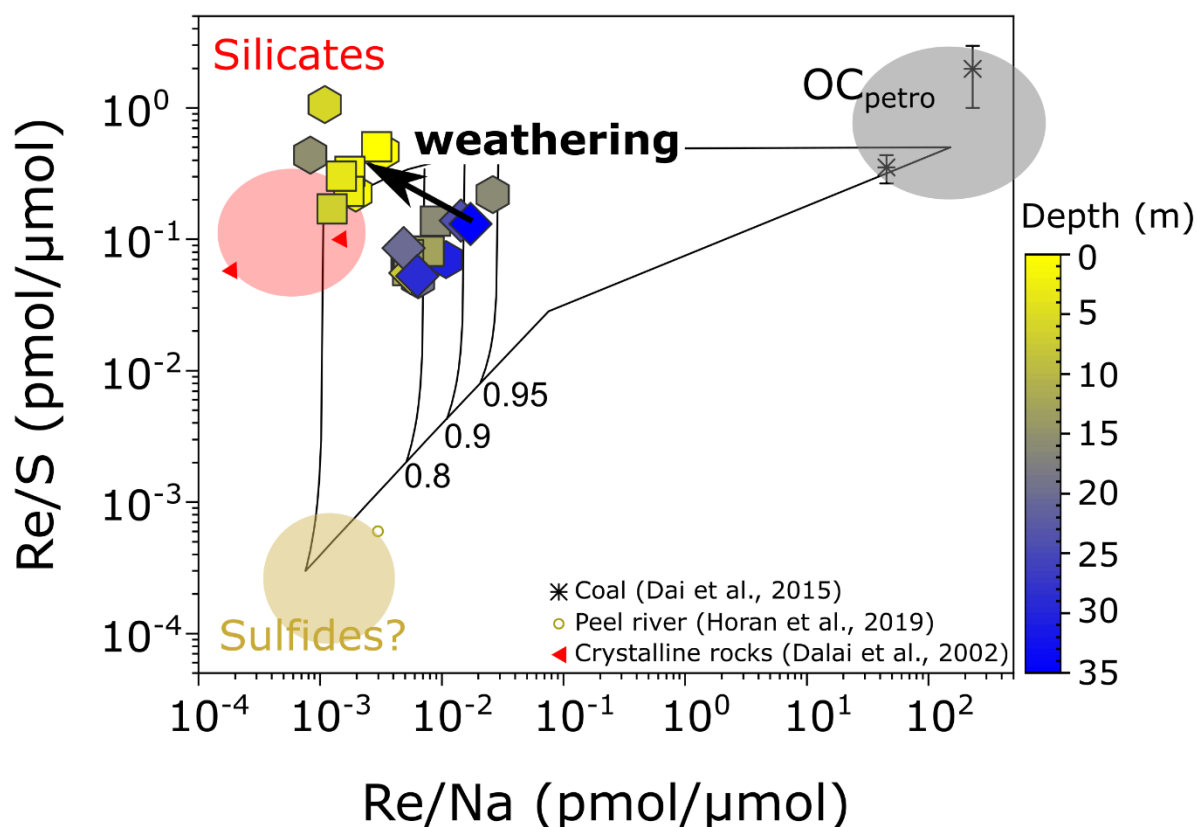


FIGURE 5 Source of rhenium at the study site using Re/Na versus Re/S ratio from the three boreholes studied here: CZMW2 (valley, squares), CZMW10 (valley, diamonds), CZMW8 (ridge, hexagons). The shaded areas represent the likely end-member composition, based on limited data available in the literature (Dalai et al., 2002; Horan et al., 2019).

Loss of Re, S and OC_{petro} through weathering

To provide further insights on the mobility of Re, S and OC_{petro} during weathering we discuss the mass transfer profiles in the ridgetop borehole (CZMW8) (Figure 3, Figure 4). While direct comparison is challenging because of a lower number of samples analyzed for Re and OC_{petro} compared to S, we observe a broadly coincidental loss of S, OC_{petro} and Re at 15.4 m. The pyrite oxidation (S loss) front is sharp, with an abrupt change in $\tau_{\text{Zr,S}}$ from -0.99 to +0.20 over a vertical distance of ~ 1 m (Figure

3a). The depletion of OC_{petro} across the weathering front appears more gradual (Figure 4b), albeit with lower sample resolution, with $\tau_{Zr,OC_{\text{petro}}}$ values from -0.36 to +0.22 over a longer vertical distance of ~ 6 m. The number of samples for Re at this depth make the comparison harder, but the Re loss profile shows a gradual increase over ~ 6 m from -0.93 to -0.53 (Figure 3c), similar to the OC_{petro} profile.

A decoupling of S loss from OC_{petro} loss has been reported in other shale weathering profiles (Jaffe et al., 2002; Gu and Brantley, 2022), with the S oxidation front being deeper than the coupled Re and OC_{petro} oxidation. The deeper S front than OC_{petro} oxidation front presumably reflects the faster reaction kinetics of pyrite (Petsch et al., 2000; Gu and Brantley, 2022). However, this assumes that O_2 in air and water has access to phases in the subsurface. This may not be the case at Shale Hills, where the generation of porosity and permeability is inherently linked to chemical weathering processes themselves (Gu et al., 2020a, 2020b). At SSH-CZO, previous work has suggested the oxidation of pyrite minerals plays a crucial role in subsequent oxidative weathering and acid hydrolysis reactions (Brantley et al., 2013; Gu et al., 2020a). This is because pyrite oxidation produces sulfuric acid, an acid that can dissolve both carbonates and clay minerals, resulting in increased pore space in the weathered matrix (Gu et al., 2020b). After pyrite is completely exhausted from the saprock, oxygen can more effectively enter through the new porosity, reacting with the remaining rock matrix (Jin et al., 2010; Brantley et al., 2013; Gu et al.,

2020a). This may explain the link between the depths of S, OC_{petro} and Re depletion.

The observed lower degree of OC_{petro} loss compared to the Re and S loss in the surface samples could come about by incomplete OC_{petro} oxidation. The slight metamorphic alteration of the Rose Hill shale (Gu et al., 2020b) could have thermally matured the organic matter in the rock, making the OC in the rock more resistant to weathering (Petsch, 2014). Alternatively, association of OC_{petro} or its weathered products with clay minerals may protect them from further oxidation (Hemingway et al., 2019; Gu and Brantley, 2022).

Long-term OC_{petro} oxidation rates

Depletion profiles of Re (Figure 3c) and OC_{petro} (Figure 4b) in the borehole samples can be used to quantify OC_{petro} oxidation rate that occurred over the timescales of the weathering profile formation, and by inference, estimate the release of CO₂ from sedimentary rock weathering. We find evidence for OC_{petro} loss at a weathering front, which could correspond to a CO₂ release over the timescales of weathering front formation, quantified by:

$$J_{OC_{petro}} = \omega \times \frac{([OC_{petro}]_p - [OC_{petro}]_s)}{100} \times \rho_P \quad (2)$$

where ω is denudation rate (10-25 m Myr⁻¹; West et al., 2013), [OC_{petro}]_p is the concentration below the reaction front (0.04±2σ%) and [OC_{petro}]_s is the concentration above the weathering front (0.02±2σ %). Density of the

protolith samples (ρ_P) is 2.7 g cm^{-3} (Gu et al., 2020b). Using these values, the OC_{petro} weathering at Shale Hills is estimated between 2.0×10^{-3} and $1.7 \times 10^{-2} \text{ tC km}^{-2} \text{ yr}^{-1}$, the range reflecting the uncertainty on the quantification of OC_{petro} (Section 4.1) and denudation rate at this site.

The trace element Re has been more precisely determined in these OC-poor samples. To apply the Re proxy to track OC_{petro} oxidation rates ($J_{\text{OCpetro-Re}}$), the following Equation 3 is used:

$$J_{\text{OCpetro-Re}} = \omega \times \frac{([\text{Re}]_p - [\text{Re}]_s)}{[\frac{\text{Re}}{\text{OC}}]_{\text{petro}}} \times F_{\text{Re-OC}} \times \rho_P \quad (3)$$

where $F_{\text{Re-OC}}$ is the fraction of Re derived from $\text{OC}_{\text{petro}} = 83 \pm 6\%$ (Figure 5). The $[\text{Re/OC}]_{\text{petro}}$ and $[\text{Re}]_p$ are the ratio and Re concentration below the weathering front, $4.3 \times 10^{-7} \text{ g g}^{-1}$ and 0.11 ppb, respectively and $[\text{Re}]_s$ is the Re concentration above the front (0.02 ppb). The long-term OC_{petro} emissions at Shale Hills determined by the Re proxy are estimated between 4.4×10^{-3} and $1.3 \times 10^{-2} \text{ tC km}^{-2} \text{ yr}^{-1}$, reflecting uncertainty on the denudation rate estimates and the $[\text{Re/OC}]_{\text{petro}}$ ratios of the protolith samples. In the protolith samples from the CZMW8 borehole, $[\text{Re/OC}]_{\text{petro}}$ varies between $3.1 \times 10^{-7} \text{ g g}^{-1}$ and $8.1 \times 10^{-7} \text{ g g}^{-1}$. Globally, this ratio can vary in a range between 10^{-7} g g^{-1} and 10^{-8} g g^{-1} across different sedimentary environments (Peucker-Ehrenbrink and Hannigan, 2000; Jaffe et al., 2002; Ross and Bustin, 2009; Sheen et al., 2018).

A previous estimate of CO_2 release from OC_{petro} oxidation at Shale Hills by Jin et al. (2014) assumed that all TOC in the bedrock was depleted

by weathering during soil production (20 mM yr^{-1} , Ma et al., 2010). The corresponding CO_2 release rate was $1.5 \times 10^{-2} \text{ tC km}^{-2} \text{ yr}^{-1}$ (Jin et al., 2014), which is broadly similar, given uncertainties, to our maximum estimates presented above, using OC_{petro} loss ($1.7 \times 10^{-2} \text{ tC km}^{-2} \text{ yr}^{-1}$) and the Re proxy ($1.3 \times 10^{-2} \text{ tC km}^{-2} \text{ yr}^{-1}$).

The OC_{petro} oxidation rate at Shale Hills is expected to be low for two reasons: i) the shale is OC_{petro} -depleted; and ii) denudation rates are extremely low. Numerical models of OC_{petro} oxidation, constrained by the reactivity of coal from abiotic laboratory incubations (Chang and Berner, 1999), suggest that OC_{petro} oxidation is limited by supply of fresh, un-oxidized material (Bolton et al., 2006). Dissolved Re fluxes from catchments in Taiwan and New Zealand confirm this, showing increases in erosion are linked to increases in OC_{petro} weathering (Hilton et al., 2014; Horan et al., 2017). OC_{petro} oxidation at Shale Hills is 2 to 3 orders of magnitude lower than OC_{petro} oxidation rates based on the dissolved Re proxy in high erosive catchments of the Himalaya (Dalai et al., 2002), Taiwan (Hilton et al., 2014), New Zealand (Horan et al., 2017), and the Mackenzie river system (Horan et al., 2019) (Figure 6).

The SSH-CZO OC_{petro} oxidation estimate reaffirms that supply of OC_{petro} to the weathering zone is a key driver of OC_{petro} oxidation on a global scale (Figure 6). The observed variability in Figure 6 may be associated with variable OC_{petro} concentrations and weathering intensity (χ), which can vary between different settings (Hilton and West, 2020). The weathering of OC_{petro} may be locally limited by temperature (Soulet et al., 2021), oxygen

supply (Bolton et al., 2006), microbial activity (Hemingway et al., 2018), and/or the particle size of OC_{petro} (Gu and Brantley, 2022). These processes could be tracked with time-series data for reaction products in the weathering zone and may be most important in erosive settings where sediment supply to the near surface environment is high.

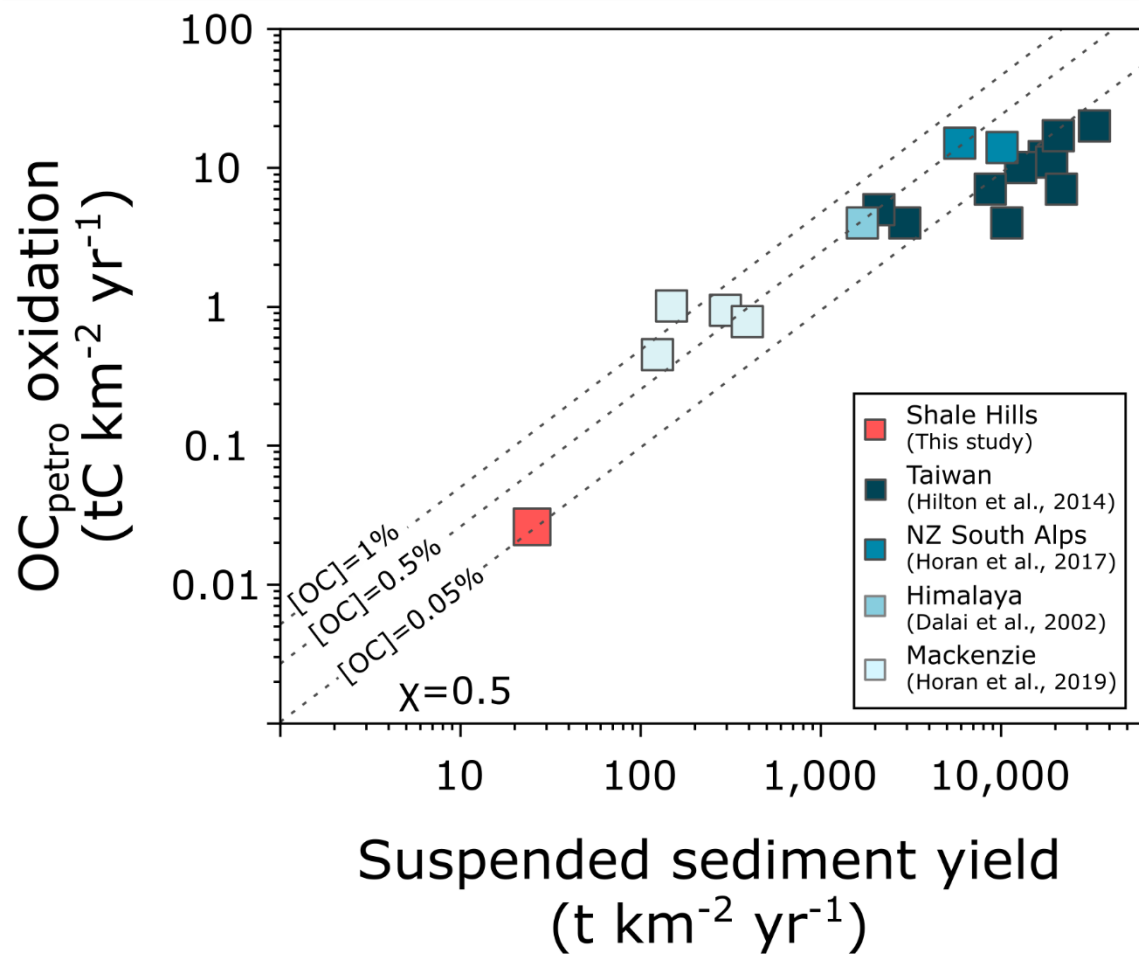


FIGURE 6 Global compilation of the control of erosion on OC_{petro} oxidation rates ($tC\ km^{-2}\ yr^{-1}$) determined with the Re proxy. The suspended sediment yield is a proxy for erosion rate. For Shale Hills, the suspended sediment yield is estimated from the long-term denudation rate estimates (Ma et al., 2011). The stippled lines represent expected weathering rates for various initial organic carbon contents (as shown) and a weathering intensity (χ) of 50%.

751 Adecoupling of stream water Re from deep weathering

752 Stream water Re concentrations are high at SSH-CZO (Table 2), despite
753 the very deep Re weathering front and relatively low Re concentrations of
754 the protolith (Figure 3). Previous work has suggested that dissolved Re
755 could be influenced by anthropogenic perturbation of the Re cycle (Miller et
756 al., 2011; Rahaman et al., 2012). Here we explore its role at Shale Hills,
757 where denudation rates and OC_{petro} contents are low. We take advantage
758 of our precise characterization of Re content in bedrock, soils and water to
759 build a dissolved-particulate mass budget to quantify the Re contribution
760 from weathering vs. anthropogenic inputs in the present day.

761 To assess the surface cycling of Re in this catchment, the present-
762 day Re flux in stream water leaving the catchment (Re_{stream}, pmol m⁻² yr⁻¹)
763 is estimated using the discharge-weighted average (Equation 4):

$$Re_{stream} = \frac{\overline{Re} \times \overline{Q_i}}{\overline{Q_a}} \times \overline{Q_a} \quad (4)$$

764 where Re (pmol l⁻¹) is Re concentration measured in stream water over the
765 sampling period, Q_i (l s⁻¹) is the instantaneous discharge measure at the
766 time of sample collection (Table 2), and $\overline{Q_a}$ is the mean annual stream
767 discharge. Using the long term mean annual discharge (2008-2015) as $\overline{Q_a}$
768 (1.07 l s⁻¹) gives dissolved Re flux estimate of 2.1×10³ pmol m⁻² yr⁻¹. The
769 $\overline{Q_a}$ over our sampling period (2018-2019) was higher at 2.27 l s⁻¹, meaning
770 the annual Re flux from June 2018 to June 2019 may have been closer to
771 4.4×10³ pmol m⁻² yr⁻¹.

We can compare this flux to an estimate of how much Re is produced by weathering of the protolith (Re_{CW} ; $\text{pmol m}^{-2} \text{ yr}^{-1}$), using Equation 5.

$$Re_{CW} = ([\overline{Re}]_p - [\overline{Re}]_s) \times \rho_p \times \omega \quad (5)$$

Here the mean Re concentration in the protolith ($[\overline{Re}]_p$) and the saprock ($[\overline{Re}]_s$) are used. Other terms are defined in Equation 3. The expected release of Re due to weathering of the protolith (Re_{CW}) is between 0.02 and $0.05 \times 10^3 \text{ pmol m}^{-2} \text{ yr}^{-1}$, the range reflecting variability in the denudation rate estimates. This is <3% of the dissolved Re flux from the stream, suggesting a negligible contribution of dissolved Re from chemical weathering.

To explore this stark decoupling of weathering inputs and dissolved exports, we turn to the precipitation and surface soil samples. The area surrounding the Shale Hills is known for coal burning activities, with a number of historical iron furnaces, fueled by local Pennsylvania coal (Herndon et al., 2011; Kraepiel et al., 2015). Furthermore, contemporary coal power plants are located upwind of the catchment (Lima et al., 2005; Ma et al., 2014). During coal combustion (500–700 °C), Re may be volatilized and released to the atmosphere as Re_2O_7 (Colodner et al., 1995). It can then be deposited on the surrounding landscapes through either wet or dry deposition (Novo et al., 2015). The abundance of Re in coal fly ash, a by-product of coal burning, may be high, as suggested by high Re concentration (5.2 ppb) measured in a Coal Fly Ash standard reference

material 1633a (product of Pennsylvania and West Virginia coals) for this study.

The present-day atmospheric Re flux (Re_{Atm}) can be estimated by multiplying the average Re concentration of precipitation samples ($1.28 \pm 0.99 \text{ pmol l}^{-1}$) with the mean annual precipitation for Shale Hills, of 1070 mm yr^{-1} (Jin et al., 2014). A present-day atmospheric deposition of Re at Shale Hills is $1.4 \pm 1.1 \times 10^3 \text{ pmol m}^{-2} \text{ yr}^{-1}$ (Figure 7). By itself, the modern Re input from precipitation is almost 20-times the chemical weathering supply of Re. Precipitation inputs can account for ~60% of the long term (2008-2015) Re flux estimate in this small catchment.

Additional insight comes from shallow groundwater samples, which have elevated Re concentrations (Table 2), suggesting inputs from surface soils, where rainfall events may leach previously deposited Re. These observations suggest that past deposition of Re on the landscape may have been higher, as recently observed for atmospheric deposition of sulfate at the study site (Shaughnessy et al., 2020). At the Shale Hills catchment, the surface soils appear to act as a temporary Re reservoir enriched in anthropogenic Re, suggesting that the present-day Re cycle in the dissolved load has been perturbed by recent human activities.

Rhenium deposited in the catchment through wet or dry atmospheric deposition, might be retained in the soil through either a pH-dependent control on the Re mobility, and/or as a solid particle form which subsequently undergoes weathering and oxidation. In terms of the pH control, the perrhenate ion, ReO_4^- , can be mobilized at low pH of forest soils

at the SSH-CZO (pH 4.0 ± 0.1 on the ridge and 4.7 ± 0.2 in the valley; Jin et al., 2011; Herndon et al., 2015b). A laboratory based study by Kim et al. (2004) showed that more than 40% of ReO_4^- could be reabsorbed onto organic molecules at pH ~ 4 . Continuous acidic precipitation, with pH 4.2 – 4.4 monitored since the 1980s (NADP, 2020), but may have started as early as the 1800s (Herndon et al., 2011; Kraepiel et al., 2015) may cause absorption of Re into the forest soils at SSH-CZO. With the increasing precipitation pH over recent years (pH ~ 5.6 ; NADP Program Office, 2020), the reabsorbed Re could be leached into the surface waters, explaining the high Re concentrations in stream waters. While this mechanism is viable, we cannot rule out the role of Re-enriched particles deposited on the catchment, which subsequently release Re as they weather.

A deposition of Re on the catchment is consistent with the enrichment of Re concentration towards the top-most soil layer in a 50 cm deep soil profile (Figure 2f). Accumulation of several other metals in the top soil is also seen at the SSH-CZO, e.g. Mo and Mn (Herndon et al., 2011; Kraepiel et al., 2015), Pb (Ma et al., 2014) and Hg (Richardson et al., 2018). To further explore the behavior of Re in the surface soils we plot Re, Mo and Mn concentrations normalized to Al (Figure 7 b-d). Aluminum is not impacted by atmospheric deposition (Kraepiel et al., 2015) and is immobile in the soil profile (Kim et al., 2018). All three elemental ratios are elevated in the upper 5 cm of the soil profile, which would imply present-day inferred inputs from anthropogenic activities, i.e., coal burning, gasoline combustion, and/or steel plants) (Herndon et al., 2011). Down to 25 cm

depth, Re/Al and Mn/Al ratios decrease by a factor of ~ 4 and Mo/Al for a factor of ~ 1.5 . Below 25 cm depth, Mn/Al and Mo/Al remain constant, but Re/Al ratio further decreases. These differences probably reflect the biogeochemical processes impacting the elements. For example, oxidized Mo is soluble (MnO_4^{2-}) and mobile, like Re. However, previous studies have suggested adsorption of Mo to oxyhydroxides and/or organic compounds in soils at $\sim \text{pH } 4$ (King et al., 2018). In contrast, Mn is thought to be largely involved in bio-cycling (Herndon and Brantley, 2011; Herndon et al., 2015b) resulting in long residence times in the soil (Kraepiel et al., 2015). The precise nature of Re adsorption in soils could be explored in future studies using the Re isotopic system (Miller et al., 2015; Dellinger et al., 2020, 2021).

To explore the legacy of anthropogenic deposition of Re to the catchment soils we here provide an estimate of the time needed to deplete the accumulated Re in surface soils (turnover time). First, the total Re mass in soil per unit land surface area (pmol m^{-2}) is summarized over depth intervals (Δd) as shown in Equation 6:

$$m_{\text{Re,soil}} = \sum \Delta d \times \rho_{\text{soil}} \times [\text{Re}]_{\text{soil}} \quad (6)$$

Where $[\text{Re}]_{\text{soil}}$ is Re concentration in soil at certain depth (Table 1) and ρ_{soil} is the soil density at different intervals as reported in Lin et al. (2006). The total Re mass in the upper 50 cm of a soil profile is $1.1 \times 10^5 \text{ pmol m}^{-2}$. To explain the measured dissolved Re flux, soil leaching ($\text{Re}_{\text{leach,soil}} = \text{Re}_{\text{stream}} - \text{Re}_{\text{atm}} - \text{Re}_{\text{cw}}$) would have to contribute

863 $0.7 \times 10^3 \text{ pmol m}^{-2} \text{ yr}^{-1}$ (Figure 7a) to the long term (2008-2015) dissolved
864 Re flux. With this constraint, we can estimate the turnover time, assuming
865 this leaching of Re is constant over time and acts to deplete the surface soil
866 reservoir:

$$T_{Re} = \frac{m_{Re,soil}}{Re_{leach,soil}} \quad (7)$$

867 This returns an estimate of T_{Re} of 160 years. This is a notable timeframe
868 over which dissolved Re concentrations could be elevated.

869 This study shows that in locations where denudation rates are low
870 and atmospheric metal deposition rates are high, the surface Re cycling is
871 significantly perturbed by anthropogenic impacts. While our study covers
872 a small catchment, these findings echo global assessments suggesting that
873 the current cycling and usage of Re associated with human activities is
874 equivalent to a Re flux of $0.15 \pm 0.01 \text{ Gg yr}^{-1}$, which is three times larger
875 than the natural Re flux $0.05 \pm 0.03 \text{ Gg yr}^{-1}$ (Sen and Peucker-Ehrenbrink,
876 2012). Our study calls for future work to better constrain modern and
877 historic Re inputs to the surface of catchments, and highlights that the
878 dissolved Re proxy for OC_{petro} oxidation (Dalai et al., 2002; Hilton et al.,
879 2014) may result in overestimation in low denudation settings.

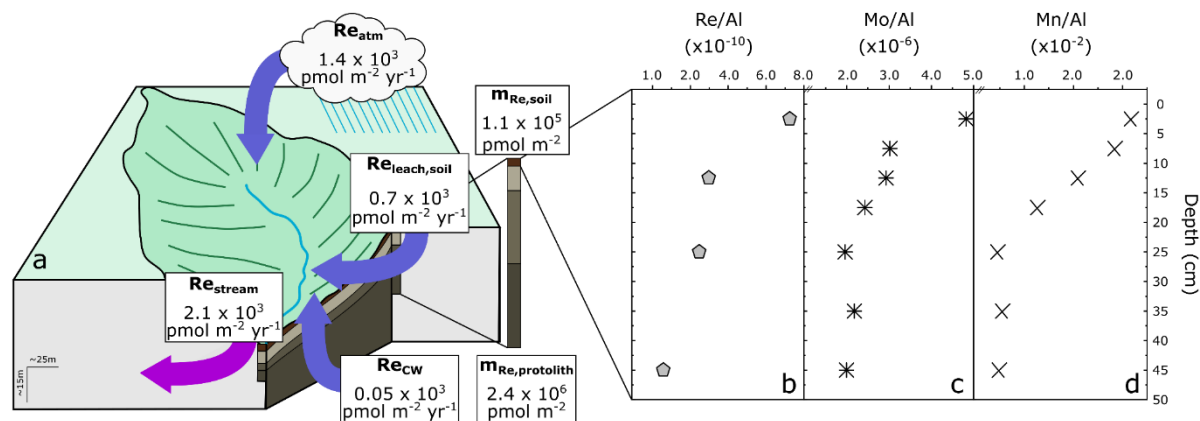


FIGURE 7 Reservoirs (pmol m^{-2}) and fluxes ($\text{pmol m}^{-2} \text{ yr}^{-1}$) of rhenium (Re) at the Shale Hills catchment.

The blue arrows represent Re input to the catchment through different geochemical processes. The purple arrow represents Re output from the catchment. Abbreviations: Re_{atm} = Re derived through present day atmospheric deposition; Re_{cw} = Re derived through chemical weathering of the protolith; $Re_{leach,soil}$ = Re leaching through surface soils; Re_{stream} = Re export from the catchment via stream discharge; $m_{Re,soil}$ = Re stock in the top 0.5 m of the surface soils; $m_{Re,protolith}$ = Re stock over 11 m of the protolith.

888 Conclusions

889 This study combines measurements of radiocarbon in the organic carbon
890 reservoir and trace element Re to examine oxidative weathering of OC_{petro}
891 in a setting experiencing low denudation. In deep weathering profiles from
892 the Susquehanna Shale Hills Critical Zone Observatory, we find evidence
893 for OC_{petro} depletion across a broad, ~6 m wide weathering front in a
894 borehole from the ridge (CZMW8), with a tau ($\tau_{Zr,OC_{petro}}$) value of
895 around -0.4. However, the measurements of radiocarbon require a deep
896 input of ^{14}C , which makes quantifying OC_{petro} loss challenging. We turn to
897 the trace element Re, and use Re/Na and Re/S ratios to estimate that
898 ~80% of Re is derived from OC_{petro} in this setting. The depletion profile of
899 Re occurs over a broad reaction front (similar to OC_{petro} front), with $\tau_{Zr,Re}$
900 between -0.77 and -0.93. In contrast, the pyrite weathering front (S loss)
901 in the ridgetop borehole appears narrower (~1 m) at a similar depth of
902 15.4 m and the S is almost fully depleted ($\tau_{Zr,S}=-0.99$). We use the OC_{petro}
903 depletion and the Re loss profiles to quantify long-term OC_{petro} oxidation
904 rates, which are low ($<1.7 \times 10^{-2}$ tC km⁻² yr⁻¹), but consistent with low
905 denudation rates (0.01–0.025 mm yr⁻¹), confirming the important role of
906 mineral supply and erosion rate on OC_{petro} oxidation.

907 We find a pronounced contrast between the deep weathering and
908 surface cycle of Re in this catchment. The low oxidative weathering rates
909 supply only small amounts of Re ($<0.05 \times 10^3$ pmol m⁻² yr⁻¹), and the

910 saprock is Re depleted. In contrast, the long term annual dissolved Re
911 export from the catchment is estimated at $2.1 \times 10^3 \text{ pmol m}^{-2} \text{ yr}^{-1}$, with
912 precipitation, shallow groundwater, and surface soils all showing elevated
913 Re concentrations. An anthropogenic Re input due to historical steel
914 production and coal burning activities can explain these patterns. Rhenium
915 may have accumulated in the surface soil and is now being slowly leached
916 to the stream waters. At the current mobilization rate, the reservoir of
917 anthropogenic Re in the surface soil could take centuries to deplete. This
918 study highlights that anthropogenic inputs of Re can be a large component
919 of the Re budget in settings with low denudation rates. It calls for renewed
920 focus on the recent perturbation of the Re cycle and how this element could
921 help elucidate the legacy of pollution impacts in catchment soils.

922 References

- 923 Anderson, S.P., Dietrich, W.E., and Brimhall, G.H., 2002, Weathering
924 profiles, mass-balance analysis, and rates of solute loss: Linkages
925 between weathering and erosion in a small, steep catchment: GSA
926 Bulletin, v. 114, p. 1143–1158, doi:10.1130/0016-
927 7606(2002)114<1143:WPMBAA>2.0.CO;2.
- 928 Berner, R.A., and Canfield, D.E., 1989, A new model for atmospheric
929 oxygen over Phanerozoic time: American Journal of Science, v. 289,
930 p. 333–361.
- 931 Bertine, K.K., and Goldberg, E.D., 1971, Fossil Fuel Combustion and the
932 Major Sedimentary Cycle: Science, v. 173, p. 233–235,
933 doi:10.1126/science.173.3993.233.
- 934 Blair, N.E., Leithold, E.L., Ford, S.T., Peeler, K.A., Holmes, J.C., and Perkey,
935 D.W., 2003, The persistence of memory: the fate of ancient
936 sedimentary organic carbon in a modern sedimentary system:
937 Geochimica et Cosmochimica Acta, v. 67, p. 63–73,
938 doi:10.1016/S0016-7037(02)01043-8.
- 939 Bolton, E.W., Berner, R.A., and Petsch, S.T., 2006, The Weathering of
940 Sedimentary Organic Matter as a Control on Atmospheric O₂: II.
941 Theoretical Modeling: American Journal of Science, v. 306, p. 575–
942 615, doi:10.2475/08.2006.01.
- 943 Brantley, S.L., Holleran, M.E., Jin, L., and Bazilevskaya, E., 2013, Probing
944 deep weathering in the Shale Hills Critical Zone Observatory,
945 Pennsylvania (USA): the hypothesis of nested chemical reaction
946 fronts in the subsurface: Earth Surface Processes and Landforms, v.
947 38, p. 1280–1298, doi:10.1002/esp.3415.
- 948 Brimhall, G.H., and Dietrich, W.E., 1987, Constitutive mass balance
949 relations between chemical composition, volume, density, porosity,
950 and strain in metasomatic hydrochemical systems: Results on
951 weathering and pedogenesis: Geochimica et Cosmochimica Acta, v.
952 51, p. 567–587, doi:10.1016/0016-7037(87)90070-6.
- 953 Burke, A. et al., 2018, Sulfur isotopes in rivers: Insights into global
954 weathering budgets, pyrite oxidation, and the modern sulfur cycle:
955 Earth and Planetary Science Letters, v. 496, p. 168–177,
956 doi:10.1016/j.epsl.2018.05.022.

- 957 Chang, S., and Berner, R.A., 1999, Coal weathering and the geochemical
958 carbon cycle: *Geochimica et Cosmochimica Acta*, v. 63, p. 3301–
959 3310, doi:10.1016/S0016-7037(99)00252-5.
- 960 Chappaz, A., Gobeil, C., and Tessier, A., 2008, Sequestration mechanisms
961 and anthropogenic inputs of rhenium in sediments from Eastern
962 Canada lakes: *Geochimica et Cosmochimica Acta*, v. 72, p. 6027–
963 6036, doi:10.1016/j.gca.2008.10.003.
- 964 Colodner, D., Edmond, J., and Boyle, E., 1995, Rhenium in the Black Sea:
965 comparison with molybdenum and uranium: *Earth and Planetary
966 Science Letters*, v. 131, p. 1–15, doi:10.1016/0012-821X(95)00010-
967 A.
- 968 Colodner, D., Sachs, J., Ravizza, G., Turekian, K., Edmond, J., and Boyle,
969 E., 1993, The geochemical cycle of rhenium: a reconnaissance: *Earth
970 and Planetary Science Letters*, v. 117, p. 205–221,
971 doi:10.1016/0012-821X(93)90127-U.
- 972 Dalai, T.K., Singh, S.K., Trivedi, J.R., and Krishnaswami, S., 2002,
973 Dissolved rhenium in the Yamuna river system and the Ganga in the
974 Himalaya: role of black shale weathering on the budgets of Re, Os,
975 and U in rivers and CO₂ in the atmosphere: *Geochimica et
976 Cosmochimica Acta*, v. 66, p. 29–43, doi:10.1016/S0016-
977 7037(01)00747-5.
- 978 Das, A., Chung, C.-H., and You, C.-F., 2012, Disproportionately high rates
979 of sulfide oxidation from mountainous river basins of Taiwan orogeny:
980 Sulfur isotope evidence: *Geophysical Research Letters*, v. 39,
981 doi:10.1029/2012GL051549.
- 982 Dellinger, M., Hilton, R.G., and Nowell, ., 2021, Fractionation of rhenium
983 isotopes in the Mackenzie River basin during oxidative weathering:
984 *Earth and Planetary Science Letters*, v. 573, p. 117131,
985 doi:10.1016/j.epsl.2021.117131.
- 986 Dellinger, M., Hilton, R.G., and Nowell, G.M., 2020, Measurements of
987 rhenium isotopic composition in low-abundance samples: *Journal of
988 Analytical Atomic Spectrometry*, v. 35, p. 377–387,
989 doi:10.1039/C9JA00288J.
- 990 Derry, L.A., and France-Lanord, C., 1996, Neogene growth of the
991 sedimentary organic carbon reservoir: *Paleoceanography*, v. 11, p.
992 267–275, doi:10.1029/95PA03839.
- 993 Galy, V., Beyssac, O., France-Lanord, C., and Eglinton, T., 2008, Recycling
994 of Graphite During Himalayan Erosion: A Geological Stabilization of
995 Carbon in the Crust: *Science*, v. 322, p. 943–945,
996 doi:10.1126/science.1161408.

997 Ghazi, L., Goñi, M., Haley, B.A., Muratli, J.M., and Pett-Ridge, J.C., 2022,
998 Concentration-runoff relationships of contrasting small mountainous
999 rivers in the Pacific Northwest, USA: Insights into the weathering of
1000 rhenium relative to other weathering products: *Geochimica et*
1001 *Cosmochimica Acta*, v. 337, p. 106–122,
1002 doi:10.1016/j.gca.2022.09.036.

1003 Grant, K.E., Galy, V.V., Chadwick, O.A., and Derry, L.A., 2019, Thermal
1004 oxidation of carbon in organic matter rich volcanic soils: insights into
1005 SOC age differentiation and mineral stabilization: *Biogeochemistry*,
1006 v. 144, p. 291–304, doi:10.1007/s10533-019-00586-1.

1007 Gu, X., and Brantley, S.L., 2022, How Particle Size Influences Oxidation of
1008 Ancient Organic Matter during Weathering of Black Shale: *ACS Earth*
1009 *and Space Chemistry*, v. 6, p. 1443–1459,
1010 doi:10.1021/acsearthspacechem.1c00442.

1011 Gu, X., Mavko, G., Ma, L., Oakley, D., Accardo, N., Carr, B.J., Nyblade,
1012 A.A., and Brantley, S.L., 2020a, Seismic refraction tracks porosity
1013 generation and possible CO₂ production at depth under a headwater
1014 catchment: *Proceedings of the National Academy of Sciences*, v. 117,
1015 p. 18991–18997, doi:10.1073/pnas.2003451117.

1016 Gu, X., Rempe, D.M., Dietrich, W.E., West, A.J., Lin, T.-C., Jin, L., and
1017 Brantley, S.L., 2020b, Chemical reactions, porosity, and
1018 microfracturing in shale during weathering: The effect of erosion rate:
1019 *Geochimica et Cosmochimica Acta*, v. 269, p. 63–100,
1020 doi:10.1016/j.gca.2019.09.044.

1021 Hemingway, J.D., Galy, V.V., Gagnon, A.R., Grant, K.E., Rosengard, S.Z.,
1022 Soulet, G., Zigah, P.K., and McNichol, A.P., 2017, Assessing the Blank
1023 Carbon Contribution, Isotope Mass Balance, and Kinetic Isotope
1024 Fractionation of the Ramped Pyrolysis/Oxidation Instrument at
1025 NOSAMS: *Radiocarbon*, v. 59, p. 179–193, doi:10.1017/RDC.2017.3.

1026 Hemingway, J.D., Hilton, R.G., Hovius, N., Eglinton, T.I., Haghipour, N.,
1027 Wacker, L., Chen, M.-C., and Galy, V.V., 2018, Microbial oxidation of
1028 lithospheric organic carbon in rapidly eroding tropical mountain soils:
1029 *Science*, v. 360, p. 209–212, doi:10.1126/science.aao6463.

1030 Hemingway, J.D., Rothman, D.H., Grant, K.E., Rosengard, S.Z., Eglinton,
1031 T.I., Derry, L.A., and Galy, V.V., 2019, Mineral protection regulates
1032 long-term global preservation of natural organic carbon: *Nature*, v.
1033 570, p. 228–231, doi:10.1038/s41586-019-1280-6.

1034 Herndon, E.M., and Brantley, S.L., 2011, Movement of manganese
1035 contamination through the Critical Zone: *Applied Geochemistry*, v.
1036 26, p. S40–S43, doi:10.1016/j.apgeochem.2011.03.024.

1037 Herndon, E.M., Dere, A.L., Sullivan, P.L., Norris, D., Reynolds, B., and
 1038 Brantley, S.L., 2015a, Landscape heterogeneity drives contrasting
 1039 concentration–discharge relationships in shale headwater
 1040 catchments: *Hydrology and Earth System Sciences*, v. 19, p. 3333–
 1041 3347, doi:10.5194/hess-19-3333-2015.

1042 Herndon, E.M., Jin, L., Andrews, D.M., Eissenstat, D.M., and Brantley, S.L.,
 1043 2015b, Importance of vegetation for manganese cycling in temperate
 1044 forested watersheds: *Biogeochemistry of Mn contaminants: Global
 1045 Biogeochemical Cycles*, v. 29, p. 160–174,
 1046 doi:10.1002/2014GB004858.

1047 Herndon, E.M., Jin, L., and Brantley, S.L., 2011, Soils Reveal Widespread
 1048 Manganese Enrichment from Industrial Inputs: *Environmental
 1049 Science & Technology*, v. 45, p. 241–247, doi:10.1021/es102001w.

1050 Hilton, R.G., Gaillardet, J., Calmels, D., and Birck, J.-L., 2014, Geological
 1051 respiration of a mountain belt revealed by the trace element rhenium:
 1052 *Earth and Planetary Science Letters*, v. 403, p. 27–36,
 1053 doi:10.1016/j.epsl.2014.06.021.

1054 Hilton, R.G., Turowski, J.M., Winnick, M., Dellinger, M., Schleppe, P.,
 1055 Williams, K.H., Lawrence, C.R., Maher, K., West, M., and Hayton, A.,
 1056 2021, Concentration-Discharge Relationships of Dissolved Rhenium in
 1057 Alpine Catchments Reveal Its Use as a Tracer of Oxidative
 1058 Weathering: *Water Resources Research*, v. 57,
 1059 doi:10.1029/2021WR029844.

1060 Hilton, R.G., and West, A.J., 2020, Mountains, erosion and the carbon
 1061 cycle: *Nature Reviews Earth & Environment*, v. 1, p. 284–299,
 1062 doi:10.1038/s43017-020-0058-6.

1063 Horan, K. et al., 2019, Carbon dioxide emissions by rock organic carbon
 1064 oxidation and the net geochemical carbon budget of the Mackenzie
 1065 River Basin: *American Journal of Science*, v. 319, p. 473–499,
 1066 doi:10.2475/06.2019.02.

1067 Horan, K., 2018, The oxidative weathering of organic matter and its carbon
 1068 dioxide emissions: Insight from the trace elements rhenium and
 1069 molybdenum [PhD]: Durham University, 244 p.,
 1070 <http://etheses.dur.ac.uk/12663/>.

1071 Horan, K., Hilton, R.G., Selby, D., Ottley, C.J., Gröcke, D.R., Hicks, M., and
 1072 Burton, K.W., 2017, Mountain glaciation drives rapid oxidation of
 1073 rock-bound organic carbon: *Science Advances*, v. 3, p. e1701107,
 1074 doi:10.1126/sciadv.1701107.

1075 Jaffe, L.A., Peucker-Ehrenbrink, B., and Petsch, S.T., 2002, Mobility of
 1076 rhenium, platinum group elements and organic carbon during black

1077 shale weathering: *Earth and Planetary Science Letters*, v. 198, p.
1078 339–353, doi:10.1016/S0012-821X(02)00526-5.

1079 Jin, L., Andrews, D.M., Holmes, G.H., Lin, H., and Brantley, S.L., 2011,
1080 Opening the “Black Box”: Water Chemistry Reveals Hydrological
1081 Controls on Weathering in the Susquehanna Shale Hills Critical Zone
1082 Observatory: *Vadose Zone Journal*, v. 10, p. 928–942,
1083 doi:10.2136/vzj2010.0133.

1084 Jin, L., Ogrinc, N., Yesavage, T., Hasenmueller, E.A., Ma, L., Sullivan, P.L.,
1085 Kaye, J., Duffy, C., and Brantley, S.L., 2014, The CO₂ consumption
1086 potential during gray shale weathering: Insights from the evolution
1087 of carbon isotopes in the Susquehanna Shale Hills critical zone
1088 observatory: *Geochimica et Cosmochimica Acta*, v. 142, p. 260–280,
1089 doi:10.1016/j.gca.2014.07.006.

1090 Jin, L., Ravello, R., Ketchum, B., Bierman, P.R., Heaney, P., White, T., and
1091 Brantley, S.L., 2010, Mineral weathering and elemental transport
1092 during hillslope evolution at the Susquehanna/Shale Hills Critical
1093 Zone Observatory: *Geochimica et Cosmochimica Acta*, v. 74, p.
1094 3669–3691, doi:10.1016/j.gca.2010.03.036.

1095 Jochum, K.P., Weis, U., Schwager, B., Stoll, B., Wilson, S.A., Haug, G.H.,
1096 Andrae, M.O., and Enzweiler, J., 2016, Reference Values Following
1097 ISO Guidelines for Frequently Requested Rock Reference Materials:
1098 *Geostandards and Geoanalytical Research*, v. 40, p. 333–350,
1099 doi:10.1111/j.1751-908X.2015.00392.x.

1100 Kim, E., Benedetti, M.F., and Boulègue, J., 2004, Removal of dissolved
1101 rhenium by sorption onto organic polymers: study of rhenium as an
1102 analogue of radioactive technetium: *Water Research*, v. 38, p. 448–
1103 454, doi:10.1016/j.watres.2003.09.033.

1104 Kim, H., Gu, X., and Brantley, S.L., 2018, Particle fluxes in groundwater
1105 change subsurface shale rock chemistry over geologic time: *Earth
1106 and Planetary Science Letters*, v. 500, p. 180–191,
1107 doi:10.1016/j.epsl.2018.07.031.

1108 King, E.K., Perakis, S.S., and Pett-Ridge, J.C., 2018, Molybdenum isotope
1109 fractionation during adsorption to organic matter: *Geochimica et
1110 Cosmochimica Acta*, v. 222, p. 584–598,
1111 doi:10.1016/j.gca.2017.11.014.

1112 Kraepiel, A.M.L., Dere, A.L., Herndon, E.M., and Brantley, S.L., 2015,
1113 Natural and anthropogenic processes contributing to metal
1114 enrichment in surface soils of central Pennsylvania: *Biogeochemistry*,
1115 v. 123, p. 265–283, doi:10.1007/s10533-015-0068-5.

- 1116 Larsen, I.J., Montgomery, D.R., and Greenberg, H.M., 2014, The
1117 contribution of mountains to global denudation: *Geology*, v. 42, p.
1118 527–530, doi:10.1130/G35136.1.
- 1119 Lima, A.L., Bergquist, B.A., Boyle, E.A., Reuer, M.K., Dudas, F.O., Reddy,
1120 C.M., and Eglinton, T.I., 2005, High-resolution historical records from
1121 Pettaquamscutt River basin sediments: 2. Pb isotopes reveal a
1122 potential new stratigraphic marker: *Geochimica et Cosmochimica*
1123 *Acta*, v. 69, p. 1813–1824, doi:10.1016/j.gca.2004.10.008.
- 1124 Lin, H.S., Kogelmann, W., Walker, C., and Bruns, M.A., 2006, Soil moisture
1125 patterns in a forested catchment: A hydropedological perspective:
1126 *Geoderma*, v. 131, p. 345–368,
1127 doi:10.1016/j.geoderma.2005.03.013.
- 1128 Ma, L., Chabaux, F., Pelt, E., Blaes, E., Jin, L., and Brantley, S., 2010,
1129 Regolith production rates calculated with uranium-series isotopes at
1130 Susquehanna/Shale Hills Critical Zone Observatory: *Earth and*
1131 *Planetary Science Letters*, v. 297, p. 211–225,
1132 doi:10.1016/j.epsl.2010.06.022.
- 1133 Ma, L., Konter, J., Herndon, E., Jin, L., Steinhoefel, G., Sanchez, D., and
1134 Brantley, S., 2014, Quantifying an early signature of the industrial
1135 revolution from lead concentrations and isotopes in soils of
1136 Pennsylvania, USA: *Anthropocene*, v. 7, p. 16–29,
1137 doi:10.1016/j.ancene.2014.12.003.
- 1138 Marin-Spiotta, E., Chadwick, O.A., Kramer, M., and Carbone, M.S., 2011,
1139 Carbon delivery to deep mineral horizons in Hawaiian rain forest soils:
1140 *Journal of Geophysical Research*, v. 116,
1141 doi:10.1029/2010JG001587.
- 1142 McNichol, A.P., Osborne, E.A., Gagnon, A.R., Fry, B., and Jones, G.A., 1994,
1143 TIC, TOC, DIC, DOC, PIC, POC — unique aspects in the preparation
1144 of oceanographic samples for ^{14}C -AMS: *Nuclear Instruments and*
1145 *Methods in Physics Research Section B: Beam Interactions with*
1146 *Materials and Atoms*, v. 92, p. 162–165, doi:10.1016/0168-
1147 583X(94)95998-6.
- 1148 Meisel, T., and Moser, J., 2004, Reference materials for geochemical PGE
1149 analysis: new analytical data for Ru, Rh, Pd, Os, Ir, Pt and Re by
1150 isotope dilution ICP-MS in 11 geological reference materials:
1151 *Chemical Geology*, v. 208, p. 319–338,
1152 doi:10.1016/j.chemgeo.2004.04.019.
- 1153 Miller, C.A., Peucker-Ehrenbrink, B., and Schauble, E.A., 2015, Theoretical
1154 modeling of rhenium isotope fractionation, natural variations across
1155 a black shale weathering profile, and potential as a paleoredox proxy:

1156 Earth and Planetary Science Letters, v. 430, p. 339–348,
1157 doi:10.1016/j.epsl.2015.08.008.

1158 Miller, C.A., Peucker-Ehrenbrink, B., Walker, B.D., and Marcantonio, F.,
1159 2011, Re-assessing the surface cycling of molybdenum and rhenium:
1160 Geochimica et Cosmochimica Acta, v. 75, p. 7146–7179,
1161 doi:10.1016/j.gca.2011.09.005.

1162 Morford, J.L., Martin, W.R., and Carney, C.M., 2012, Rhenium geochemical
1163 cycling: Insights from continental margins: Chemical Geology, v.
1164 324–325, p. 73–86, doi:10.1016/j.chemgeo.2011.12.014.

1165 NADP Program Office, 2020, National Atmospheric Deposition Program
1166 (NRSP-3):, <http://nadp.slh.wisc.edu/>.

1167 Novo, L.A.B., Mahler, C.F., and González, L., 2015, Plants to harvest
1168 rhenium: scientific and economic viability: Environmental Chemistry
1169 Letters, v. 13, p. 439–445, doi:10.1007/s10311-015-0517-3.

1170 Ogrič, M., 2021, Chemical weathering of sedimentary rocks as a source of
1171 carbon dioxide to the atmosphere: Durham Univeristy,
1172 <http://etheses.dur.ac.uk/14179/>.

1173 Petsch, S.T., 2014, Weathering of Organic Carbon, *in* Holland, H.D. and
1174 Turekian, K.K. eds., Treatise on Geochemistry (Second Edition),
1175 Oxford, Elsevier, p. 217–238, doi:10.1016/B978-0-08-095975-
1176 7.01013-5.

1177 Petsch, S.T., Berner, R.A., and Eglinton, T.I., 2000, A field study of the
1178 chemical weathering of ancient sedimentary organic matter: Organic
1179 Geochemistry, v. 31, p. 475–487, doi:10.1016/S0146-
1180 6380(00)00014-0.

1181 Peucker-Ehrenbrink, B., and Hannigan, R.E., 2000, Effects of black shale
1182 weathering on the mobility of rhenium and platinum group elements:
1183 Geology, v. 28, p. 475–478, doi:10.1130/0091-
1184 7613(2000)28<475:EOBSWO>2.0.CO;2.

1185 Pierson-Wickmann, A.-C., Reisberg, L., and France-Lanord, C., 2002,
1186 Behavior of Re and Os during low-temperature alteration: Results
1187 from Himalayan soils and altered black shales: Geochimica et
1188 Cosmochimica Acta, v. 66, p. 1539–1548, doi:10.1016/S0016-
1189 7037(01)00865-1.

1190 Plank, T., and Manning, C.E., 2019, Subducting carbon: Nature, v. 574, p.
1191 343–352, doi:10.1038/s41586-019-1643-z.

1192 Prouty, N.G., Roark, E.B., Koenig, A.E., Demopoulos, A.W.J., Batista, F.C.,
1193 Kocar, B.D., Selby, D., McCarthy, M.D., Mienis, F., and Ross, S.W.,

1194 2014, Deep-sea coral record of human impact on watershed quality
 1195 in the Mississippi River Basin: *Global Biogeochemical Cycles*, v. 28,
 1196 p. 29–43, doi:10.1002/2013GB004754.

1197 Rahaman, W., Singh, S.K., and Shukla, A.D., 2012, Rhenium in Indian
 1198 rivers: Sources, fluxes, and contribution to oceanic budget:
 1199 *Geochemistry, Geophysics, Geosystems*, v. 13,
 1200 doi:10.1029/2012GC004083.

1201 Richardson, J.B., Aguirre, A.A., Buss, H.L., Toby O’Geen, A., Gu, X., Rempe,
 1202 D.M., and Richter, D. de B., 2018, Mercury Sourcing and
 1203 Sequestration in Weathering Profiles at Six Critical Zone
 1204 Observatories: *Global Biogeochemical Cycles*, v. 32, p. 1542–1555,
 1205 doi:10.1029/2018GB005974.

1206 Ross, D.J.K., and Bustin, M.R., 2009, The importance of shale composition
 1207 and pore structure upon gas storage potential of shale gas reservoirs:
 1208 *Marine and Petroleum Geology*, v. 26, p. 916–927,
 1209 doi:10.1016/j.marpetgeo.2008.06.004.

1210 Schwab, V.F. et al., 2019, ¹⁴C-Free Carbon Is a Major Contributor to
 1211 Cellular Biomass in Geochemically Distinct Groundwater of Shallow
 1212 Sedimentary Bedrock Aquifers: *Water Resources Research*, v. 55, p.
 1213 2104–2121, doi:10.1029/2017WR022067.

1214 Selby, D., and Creaser, R.A., 2003, Re–Os geochronology of organic rich
 1215 sediments: an evaluation of organic matter analysis methods:
 1216 *Chemical Geology*, v. 200, p. 225–240, doi:10.1016/S0009-
 1217 2541(03)00199-2.

1218 Selby, D., Creaser, R.A., and Fowler, M.G., 2007, Re–Os elemental and
 1219 isotopic systematics in crude oils: *Geochimica et Cosmochimica Acta*,
 1220 v. 71, p. 378–386, doi:10.1016/j.gca.2006.09.005.

1221 Sen, I.S., and Peucker-Ehrenbrink, B., 2012, Anthropogenic Disturbance of
 1222 Element Cycles at the Earth’s Surface: *Environmental Science &
 1223 Technology*, v. 46, p. 8601–8609, doi:10.1021/es301261x.

1224 Shaughnessy, A.R., Gu, X., Wen, T., and Brantley, S.L., 2020, Machine
 1225 Learning Deciphers CO₂; Sequestration and Subsurface Flowpaths
 1226 from Stream Chemistry: *Hydrology and Earth System Sciences*,
 1227 doi:doi.org/10.5194/hess-2020-537.

1228 Shi, Y., and Xiao, D., 2019, SSHCZO -- Streamflow / Discharge -- Discharge
 1229 Reanalysis -- Shale Hills -- (2008-2015), HydroShare,
 1230 [http://www.hydroshare.org/resource/7f9c036b7d804eb3a50bdd60d](http://www.hydroshare.org/resource/7f9c036b7d804eb3a50bdd60d01bf92a)
 1231 [01bf92a](http://www.hydroshare.org/resource/7f9c036b7d804eb3a50bdd60d01bf92a).

1232 Stuiver, M., and Polach, H.A., 1977, Discussion Reporting of ^{14}C Data:
 1233 Radiocarbon, v. 19, p. 355–363, doi:10.1017/S0033822200003672.

1234 Sullivan, P.L. et al., 2016, Oxidative dissolution under the channel leads
 1235 geomorphological evolution at the Shale Hills catchment: American
 1236 Journal of Science, v. 316, p. 981–1026, doi:10.2475/10.2016.02.

1237 Torres, M.A., Moosdorf, N., Hartmann, J., Adkins, J.F., and West, A.J.,
 1238 2017, Glacial weathering, sulfide oxidation, and global carbon cycle
 1239 feedbacks: Proceedings of the National Academy of Sciences, v. 114,
 1240 p. 8716–8721, doi:10.1073/pnas.1702953114.

1241 Trumbore, S., 2009, Radiocarbon and Soil Carbon Dynamics: Annual
 1242 Review of Earth and Planetary Sciences, v. 37, p. 47–66,
 1243 doi:10.1146/annurev.earth.36.031207.124300.

1244 West, N., Kirby, E., Bierman, P., Slingerland, R., Ma, L., Rood, D., and
 1245 Brantley, S., 2013, Regolith production and transport at the
 1246 Susquehanna Shale Hills Critical Zone Observatory, Part 2: Insights
 1247 from meteoric ^{10}Be : Journal of Geophysical Research: Earth Surface,
 1248 v. 118, p. 1877–1896, doi:10.1002/jgrf.20121.

1249 Wildman, R.A., 2004, The weathering of sedimentary organic matter as a
 1250 control on atmospheric O_2 : I. Analysis of a black shale: American
 1251 Journal of Science, v. 304, p. 234–249, doi:10.2475/ajs.304.3.234.

1252 Yan, J., Manelski, R., Vasilas, B., and Jin, Y., 2018, Mobile Colloidal Organic
 1253 Carbon: An Underestimated Carbon Pool in Global Carbon Cycles?
 1254 Frontiers in Environmental Science, v. 6,
 1255 doi:10.3389/fenvs.2018.00148.

1256 Yeghicheyan, D. et al., 2013, A Compilation of Silicon, Rare Earth Element
 1257 and Twenty-One other Trace Element Concentrations in the Natural
 1258 River Water Reference Material SLRS-5 (NRC-CNRC): Geostandards
 1259 and Geoanalytical Research, v. 37, p. 449–467, doi:10.1111/j.1751-
 1260 908X.2013.00232.x.

1261

1262